

Numerical simulations of super-luminous supernovae of type IIn

Luc Dessart,¹ Edouard Audit,² and D. John Hillier³

¹: *Laboratoire Lagrange, UMR7293, Université Nice Sophia-Antipolis, CNRS, Observatoire de la Côte d’Azur, 06300 Nice, France.*

²: *CEA, Maison de la Simulation, USR 3441, CEA-CNRS-INRIA- Univ. Paris-Sud - Univ. de Versailles, 91191, Gif-sur-Yvette Cedex, France.*

³: *Department of Physics and Astronomy & Pittsburgh Particle Physics, Astrophysics, and Cosmology Center (PITT PACC), University of Pittsburgh, 3941 O’Hara Street, Pittsburgh, PA 15260, USA.*

Accepted 2015 March 18. Received 2015 March 09; in original form 2015 January 06

ABSTRACT

We present numerical simulations that include 1-D Eulerian multi-group radiation-hydrodynamics, 1-D non-Local-Thermodynamic-Equilibrium (non-LTE) radiative transfer, and 2-D polarised radiative transfer for super-luminous interacting supernovae (SNe). Our reference model is a $\sim 10 M_{\odot}$ inner shell with 10^{51} erg ramming into a $\sim 3 M_{\odot}$ cold outer shell (the circumstellar-medium, or CSM) that extends from 10^{15} to 2×10^{16} cm and moves at 100 km s^{-1} . We discuss the light curve evolution, which cannot be captured adequately with a grey approach. In these interactions, the shock-crossing time through the optically-thick CSM is much longer than the photon diffusion time. Radiation is thus continuously leaking from the shock through the CSM, in disagreement with the shell-shocked model that is often invoked. Our spectra redden with time, with a peak distribution in the near-UV during the first month gradually shifting to the optical range over the following year. Initially Balmer lines exhibit a narrow line core and the broad line wings that are characteristic of electron scattering in the SNe IIn atmospheres (CSM). At later times they also exhibit a broad blue shifted component which arises from the cold dense shell. Our model results are broadly consistent with the bolometric light curve and spectral evolution observed for SN 2010jl. Invoking a prolate pole-to-equator density ratio in the CSM, we can also reproduce the $\sim 2\%$ continuum polarisation, and line depolarisation, observed in SN 2010jl. By varying the inner shell kinetic energy and the mass and extent of the outer shell, a large range of peak luminosities and durations, broadly compatible with super-luminous SNe IIn like 2010jl or 2006gy, can be produced.

Key words: radiative transfer – radiation hydrodynamics – polarisation – supernovae: general – supernovae: individual: 2010jl

1 INTRODUCTION

Since the original identification of interacting supernovae (SNe; Dopita et al. 1984; Niemela et al. 1985) and the creation of the SN IIn class (Schlegel 1990), the sample of such peculiar Type II SNe has grown from a few to a few tens of events. It has also revealed an intriguing diversity, spanning a range of luminosities, duration, line profile morphology, with events like SNe 1988Z (Stathakis & Sadler 1991; Turatto et al. 1993), 1994W (Sollerman et al. 1998; Chugai et al. 2004), 2006gy (Smith et al. 2007), and the enigmatic SN 2009ip (Mauerhan et al. 2013; Pastorello et al. 2013; Margutti et al. 2014). The origin of Type IIn SNe is associated with the interaction of fast material with previously-expelled slowly-expanding material (Grasberg & Nadezhin 1986). The resulting shock leads to deceleration of the inner shell, acceleration of the outer shell, and conversion of kinetic energy into internal and radiative energy. Because (standard) non-interacting SNe radiate merely 1% of their total energy (the rest being kinetic), interacting SNe can easily

reach extraordinary luminosities by tapping this abundant reservoir of kinetic energy. For example, an interaction extracting 30% of a 10^{51} erg ejecta could produce a SN IIn with a luminosity of $10^{10} L_{\odot}$ for 3 months.

Super luminous interacting SNe require both a high kinetic energy in the inner shell and a large mass reservoir in the outer shell (see, e.g., Moriya et al. 2013b). Two good examples of such SNe IIn are SN 2006gy (Smith et al. 2007) and more recently SN 2010jl (Stoll et al. 2011). The latter has extensive photometric and spectroscopic observations (Stoll et al. 2011; Zhang et al. 2012; Ofek et al. 2014; Fransson et al. 2014) and also has spectropolarimetric data (Patat et al. 2011; Williams et al. 2014). How stars produce the outer shell is unclear – it may be material ejected by the pair-production instability (Barkat et al. 1967; Woosley et al. 2007) or it may be material ejected via a super-Eddington wind (Owocki et al. 2004). Here, we simply consider the interaction between a fast moving inner shell and a slowly-moving

massive outer shell, and leave aside speculations concerning their origin.

Numerical simulations of interacting SNe are generally undertaken with radiation hydrodynamics (Chugai et al. 2004; Woosley et al. 2007; Moriya et al. 2013b; Whalen et al. 2013), hydrodynamics combined with a parameterised cooling function (van Marle et al. 2010; Chen et al. 2014), or pure hydrodynamics (by assuming adiabaticity; see, e.g., Blondin et al. 1996). When studying super-luminous SNe IIn, radiation hydrodynamics with a non-grey (multi-group) treatment is a must because the radiation contribution is a sizeable fraction of the pressure/energy in the problem, the characteristic temperatures of the radiation and of the gas may differ strongly, and the emerging radiation provides essential signatures characterising the event.

The radiative transfer modelling for SNe IIn comes at present in two flavours. It is either based on the results of radiation hydrodynamics simulations but limited to a single line, e.g., $H\alpha$ (Chugai et al. 2004), or based on an ad-hoc atmospheric structure and the assumption of steady-state radiation through a diffusive optically thick inner boundary (Dessart et al. 2009).

In this work, we discuss numerical simulations for super-luminous SNe of type IIn, including studies with radiation hydrodynamics, radiative transfer, and polarised radiative transfer codes. In Section 2, we first present the multi-group 1-D Eulerian radiation hydrodynamics simulations we perform with HERACLES, including the numerical approach, the standard interaction configuration we adopt as initial conditions, and the results for both the dynamics and the radiation. We then present in Section 3 non-LTE radiative-transfer simulations with CMFGEN, which we compute for a number of snapshots using the results from the radiation-hydrodynamical modelling. We discuss line profile broadening, and the relative roles of expansion and electron scattering. In Section 4, we present polarisation calculations based on these CMFGEN simulations but artificially distorted along an axis of symmetry, in order to produce prolate density configurations. We assess the level of asymmetry needed to explain the observed continuum polarisation (and line depolarisation) reported for SN 2010jl. In Section 5, we discuss the dependency of our results on the interaction properties, varying the kinetic energy of the inner shell and the mass/extent of the circumstellar medium (CSM). Finally, in Section 6, we present our conclusions.

2 RADIATION HYDRODYNAMICS WITH HERACLES

2.1 Numerical approach

HERACLES is a Eulerian multi-dimensional radiation-hydrodynamics code (González et al. 2007), with the possibility for multi-group radiation transport (Vaytet et al. 2011). The hydrodynamics is treated using a standard second order Godunov scheme. For the radiation transfer, conduction, flux limited diffusion (FLD) and the M1 moment model (Dubroca & Feugeas 1999) are implemented in HERACLES, the latter two with the possibility of using a multi-group approach. Apart from a comparison test that uses a grey treatment, the simulations presented in this paper are all done using the multi-group M1 moment model. As explained below, a multi-group treatment is necessary in order to take into account the large opacity variations with frequency and the strong imbalance between radiation and gas temperature. The M1 model has also some strong benefit compared to the more standard FLD approach. First of all the M1 model is exact in both the

diffusion and the free-streaming limit and is rather accurate in between. It is therefore well suited to model regions with low or intermediate optical depth. Furthermore, the M1 method solves explicitly for both the energy and the flux through moments of the radiative transfer equations. The M1 model can distinguish between absorption/emission and scattering opacities. The effect of scattering in regions where the scattering opacity is dominant can then be taken into account. Finally, the radiative transfer is formulated in the co-moving frame and as is shown in Vaytet et al. (2011) the Doppler and aberrations effects are properly accounted for, which is important when large velocity gradients are present.

We use the multi-group solver because grey radiation transport, often used for simulations of non-interacting Type II SNe, is inadequate in SNe IIn. In non-interacting Type II SNe, the radiation and the gas have similar temperatures everywhere (even identical at large optical depths), so that adopting the Rosseland mean opacity, for example, is not a bad representation of the effective opacity of the material. In contrast, the radiation produced from the interaction in SNe IIn has a characteristic temperature that can vastly differ from the medium that it traverses, and the total continuum optical depth is not much in excess of about ten. In the next section, we illustrate the impact on the light curve produced by assuming a grey rather than an energy-dependent LTE opacity for the material.

In this work, we adopt a uniform composition, with a H mass fraction of 0.633, He mass fraction of 0.36564, and an iron mass fraction of 0.00136 to reflect approximately the near-solar composition of a blue or a red supergiant (hereafter BSG/RSG) star (for SN 2010jl, Stoll et al. 2011) argue for a sub-solar metallicity, which may be important for understanding how these SNe IIn come about, but is irrelevant for the present radiation-hydrodynamics considerations).

We supply the code with an opacity table for our adopted composition. We compute our opacities as a function of density, temperature and energy group. Energy groups are positioned at strategic locations to capture the strong variation in absorptive opacity with wavelength. We use one group for the entire Lyman continuum (including the X-ray range), two groups for the Balmer continuum, two for the Paschen continuum, and three groups for the Brackett continuum and beyond.¹ Our opacity code computes the LTE level populations and ionisation state of the gas, and then uses the atomic data available within CMFGEN to compute LTE opacities and to make the opacity table. The domain covered is 10^{-20} to 10^{-5} g cm⁻³ in 200 bins, and from 2000 to 500,000 K in 500 bins — we use the nearest edge for requests outside the table boundaries. Here, we consider the contribution from electron scattering and bound-free opacity for H I, He I–II, and Fe I–XII. A major limitation of our work is that we ignore line opacity and emissivity in our HERACLES simulations. Metal line blanketing (in particular from Fe) would enhance the opacity in the UV (inhibiting further the escape of UV photons). We also neglect cooling due to CNO elements, which requires a non-LTE study with specific allowance for enhanced photon escape due to the velocity field. Inclusion of these effects is left to a future study.

In Fig. 1, we plot the photon mean free path and its inverse

¹ We tried using several energy groups to cover the X-ray and the EUV ranges better but this caused numerical problems with the radiative transfer. The solver struggled converging when an exceedingly small energy/flux was present in those energy groups, a situation encountered outside of the shocked region. In practice, this should not impact our results sizeably because the optical depth to hard radiation (all Lyman photons) is huge at all times considered here.

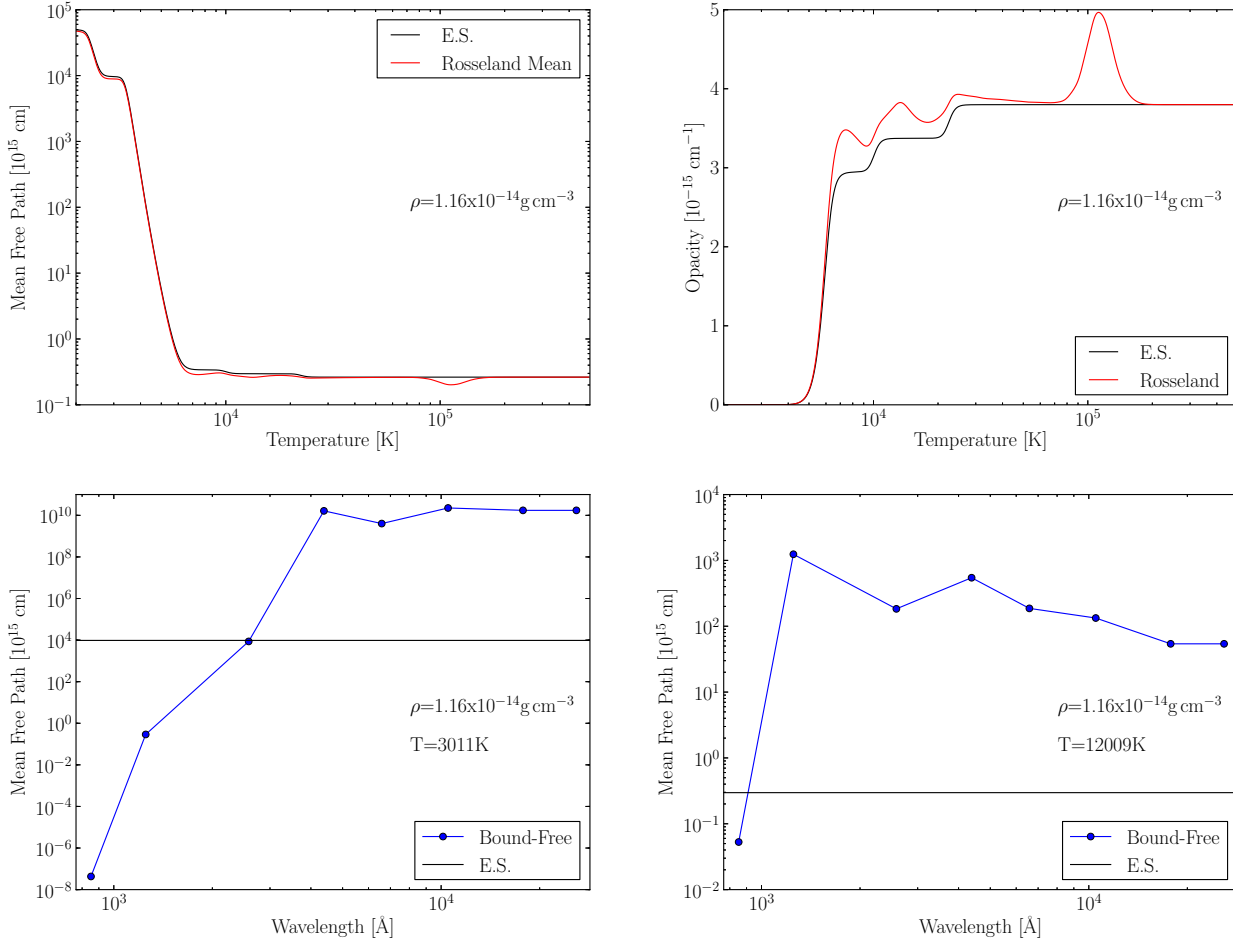


Figure 1. *Top row:* Illustration of the variation of the photon mean free path (left) and inverse mean free path (right) at a mass density of $1.16 \times 10^{-14} \text{ g cm}^{-3}$. The electron-scattering opacity (black) is the main contribution to the Rosseland-mean opacity (red; which accounts for bound-bound and bound-free processes), except in the regions of partial ionisation of H and He at 8000–20000 K and in the iron-opacity bump in the range 100000–200000 K. The precise temperature regions where these offsets occur depend on density. The most critical variation in the opacity is associated with the recombination of H and He, leading to a very small opacity at low temperature. *Bottom row:* Illustration of the wavelength dependence of the photon mean free path associated with absorptive processes (blue) at $\sim 3000 \text{ K}$ (left) and $\sim 12000 \text{ K}$ (right), corresponding to conditions in which hydrogen is neutral and ionised, respectively. The filled dots correspond to the central wavelength of each energy group used for both the opacity table and the HERACLES simulations.

(i.e., the opacity) against wavelength for different processes at different densities and temperatures. In super-luminous SNe II_n the spectrum formation region is typically optically thick in the Lyman continuum (and at X-ray wavelengths) and high-energy photons will tend to thermalise, even at low electron-scattering optical depth. Longward of the Lyman continuum, electron scattering opacity typically dominates over absorptive opacities and so low-energy photons will thermalise inefficiently at most times and locations.

The simulations in this work use an ideal gas equation of state with $\gamma = 5/3$.² We also adopt a mean atomic weight of 1.38 in all simulations. In practice, this value depends on the ionisation state of the gas, but in ways that need to be determined by using a general equation of state — this is left to a forthcoming study.

Our simulations are 1-D and use a uniform radial grid with 1600 points, covering from 0.05 to $2 \times 10^{16} \text{ cm}$. Degrading the res-

olution by a factor of four produces the same overall properties (e.g., the bolometric maximum is changed by $\sim 10\%$), although the shock is less resolved and more numerical diffusion occurs as the interaction region crosses grid zones in the course of the simulation. This has a visible impact on the properties of the forward and reverse shocks and the associated temperature jumps, but it does not influence significantly the energy solved for by HERACLES. Very high resolution simulations that yielded better resolution of the shock structure gave, for example, similar results for the properties of the CSM, the shock propagation speed, and the emergent luminosity.

The initial configuration for the interaction is determined analytically. We prescribe a density and a temperature structure for the inner shell (tagged as the SN ejecta, but the results apply to any ejected shell with similar properties) and the outer shell (we assume the CSM arises from pre-SN mass loss in the form of a wind). We adopt a structure for the SN ejecta which is based on the simulations of core-collapse SNe we perform (Dessart et al. 2010b,a), in practice comparable to the formulation of Chevalier & Irwin (2011) and Moriya et al. (2013b). In the present paper, we are only interested

² We therefore ignore the variations in thermodynamic quantities that arise from variations in ionisation.

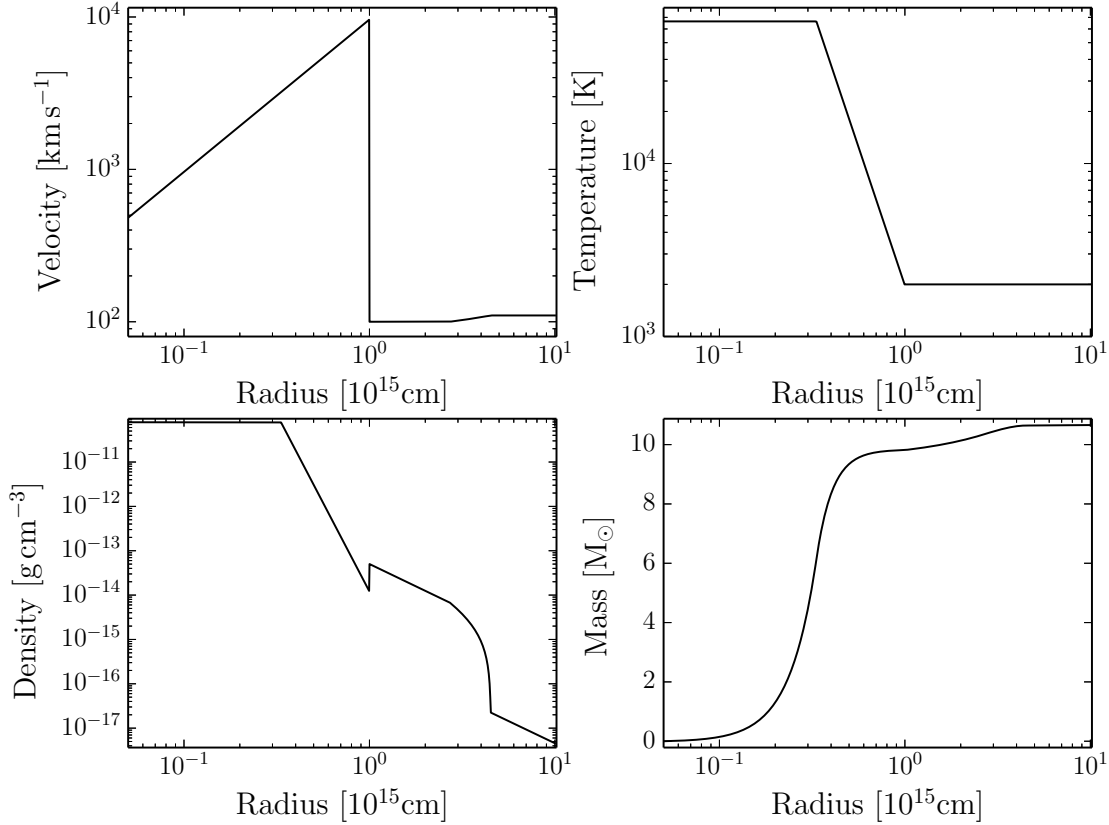


Figure 2. Initial configuration for the reference interaction model X simulated with HERACLES. We show radial profiles of the velocity, the temperature, the mass density, and the Lagrangian mass. Global quantities and additional details for this model are given in Table 1 and Section 2.1.

in studying the basic properties of super-luminous SNe II_n and thus focus on one event (i.e., SN 2010jl), for which we are guided by the parameters of Fransson et al. (2014), who argue for a SN explosion leading to interaction with a dense and extended CSM. We do not include any unstable nuclei in the simulation and thus ignore any contribution from radioactive decay.

For our standard interaction model, named X, we take a $9.8 M_{\odot}$ inner ejecta (in homologous expansion) with 10^{51} erg. Its density structure is given by a power law in radius with exponent $N_{\rho} = 8$ outside of $V_0 \sim 3000 \text{ km s}^{-1}$ and constant within it. Its temperature structure is given by a power law in density with exponent $N_T = 0.4$, rising from 2000 K at the ejecta/CSM interface radius located at R_t (we enforce a maximum temperature of 65000 K in the inner ejecta). The SN ejecta is 11.6 d old when the interaction starts. For the outer shell, which starts at $R_t = 10^{15} \text{ cm}$, we adopt a wind structure with a constant velocity of 100 km s^{-1} (and constant temperature of 2000 K), but split that space into two regions of distinct density. Below 10^{16} cm , we prescribe a mass loss rate of $0.1 M_{\odot} \text{ yr}^{-1}$, and beyond that radius we use a mass loss rate of $10^{-3} M_{\odot} \text{ yr}^{-1}$ (i.e., two orders of magnitude smaller). The motivation for this is three fold. First, the CSM mass should not be unrealistically large. By truncating the high mass loss region, we can control the total CSM mass for any chosen mass loss. Second, the phase of high mass loss in massive stars like $\eta \text{ Car}$ lasts for a period of the order of ten years, not for centuries. With our choice of outer radius and wind speed, the high mass loss phase has a duration of $\sim 28 \text{ yr}$. Third, the transition to a lower density outer region will facilitate a reduction in the luminosity at later times, as observed

in SN 2010jl past 300 d (see below, and Fransson et al. 2014). For convenience, we interpolate the density at the junction between the two shells in order to smooth the profile and avoid an overly abrupt change in luminosity when the shock reaches this region. The inner edge of the outer shell has a kinematic age of 3.2 yr. The CSM has a total mass of $2.89 M_{\odot}$ and a total kinetic energy of $5.2 \times 10^{47} \text{ erg}$. To summarise, for the SN ejecta ($R < R_t$), we adopt:

$$\begin{aligned} V(R) &= (R/R_t)V_{\max}, \\ V_0 &= V_{\max}/3, \\ \rho(V) &= \rho_0(V_0/V)^{N_{\rho}} \text{ for } V > V_0, \\ \rho(V) &= \rho_0 \text{ for } V < V_0 \text{ and} \\ T(V) &= 2000 (\rho(V)/\rho(V_{\max}))^{N_T} \text{ K}. \end{aligned}$$

The proportionality constants ρ_0 and V_{\max} are adjusted so that the total SN ejecta mass and kinetic energy match the desired values (see Table 1). For the CSM ($R > R_t$), we adopt:

$$\begin{aligned} \rho(R) &= \dot{M}/4\pi R^2 V, \\ V &= 100 \text{ km s}^{-1} \text{ and}, \\ T &= 2000 \text{ K} \end{aligned}$$

where $\dot{M} = \dot{M}_{\text{CSM,in}}$ for $R < 10^{16} \text{ cm}$ and $\dot{M} = \dot{M}_{\text{CSM,out}}$ for $R > 10^{16} \text{ cm}$.

The initial conditions for model X are shown in Fig. 2. To explore some dependencies of our results, we vary these ejecta/CSM conditions and discuss the implications in Section 5 (see also Table 1).

Table 1. Summary of simulations performed in this work. The reference model X is discussed in detail through the most part of the paper (Section 2), while additional simulations (Xe3 etc.) are discussed in Section 5. For all simulations, the minimum and maximum radii of the Eulerian grid are 5×10^{13} and 2×10^{16} cm, and the transition radius between the SN ejecta and the CSM lies at a radius R_t of 10^{15} cm. In all cases, the mass of the inner shell (the SN ejecta) is $9.8 M_\odot$, and the CSM wind velocity is 100 km s^{-1} . Results from the HERACLES simulation for each model are given in the last three columns. The time to peak is the time to reach maximum from the time when the rising bolometric luminosity is only 1% of the value at peak (this way, we cancel the light travel time to the outer boundary, where we record the flux). We finally add results from Section 3 for the bolometric correction and colour at peak. Numbers in parenthesis are powers of ten.

model	$E_{\text{kin,SN}}$ [10^{51} erg]	$V_{\text{max,SN}}$ [km s^{-1}]	$E_{\text{kin,CSM}}$ [10^{51} erg]	M_{CSM} [M_\odot]	$\dot{M}_{\text{CSM,in}}$ [$M_\odot \text{ yr}^{-1}$]	$\dot{M}_{\text{CSM,out}}$ [$M_\odot \text{ yr}^{-1}$]	$L_{\text{bol,peak}}$ [erg s^{-1}]	B.C.@peak [mag]	$(V-I)_{\text{@peak}}$ [mag]	t_{peak} [d]	$\int L dt$ [10^{51} erg]
X	1	9608	5.17(-4)	2.89	0.1	0.001	3.024(43)	-1.06	0.15	19.4	0.32
Xe3	3	16642	9.70(-4)	2.89	0.1	0.001	1.204(44)	-1.35	0.11	15.7	0.88
Xe3m6	3	16642	5.15(-3)	17.31	0.6	0.006	2.080(44)	-1.39	0.01	55.7	2.05
Xe3m6r	3	16642	6.08(-3)	26.73	0.6	0.006	1.818(44)	-1.05	0.06	68.3	2.13
Xe10	10	30384	2.55(-3)	2.89	0.1	0.001	6.399(44)	-1.46	0.13	12.7	2.92
Xe10m6	10	30384	1.31(-2)	17.31	0.6	0.006	1.091(45)	-1.80	-0.04	34.2	6.89
Xm3	1	9608	1.46(-3)	8.66	0.3	0.003	3.906(43)	-0.84	0.13	47.9	0.49
Xm6	1	9608	2.87(-3)	17.31	0.6	0.006	4.751(43)	-0.80	0.27	77.5	0.63

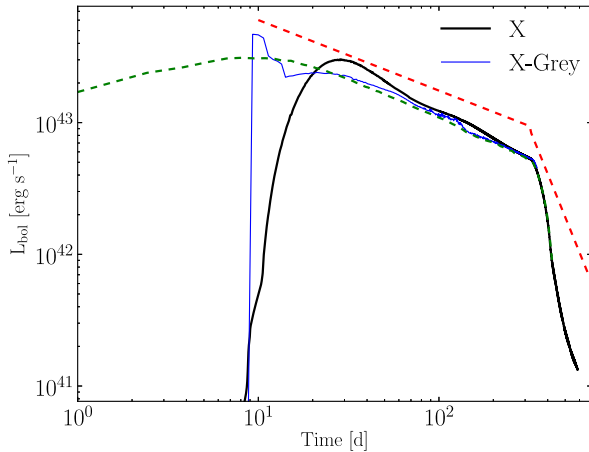


Figure 3. Bolometric light curve evolution for the SN IIIn model X (multi-group; black) and its grey counterpart (blue). We add the bolometric luminosity at the shock (green dashed curve), which differs at times $\lesssim 200$ d from the recorded bolometric luminosity because of optical depth and light travel time effects (there is an 8 d light travel time to the outer boundary from the initial location of the interaction region and a ~ 35 d diffusion time through the CSM once it has become ionised). For comparison, we show the analytical model light curve (red dashed curve) of Fransson et al. (2014) for SN 2010jl.

As the code is Eulerian, the flow constantly leaves the grid at the outer boundary. Conditions are flow out, for both the gas and the radiation. At the inner boundary, we use a reflecting condition for the radiation (zero flux). For the gas, we use an inflow condition dynamically consistent with the properties of the inner shell. We assign to this injected material a low temperature of 2000 K, a velocity that preserves the homologous expansion of the inner shell material ($V \propto R$), and a density $\rho_{\text{ib}} = \rho_1 x^3$, with $x = t/(t + dt)$, and where ρ_1 is the density in the first active zone, $t = R_{\text{ib}}/V_{\text{ib}}$, and dt is the time step. The injected material has no dynamical or radiative influence on the physics of the interaction and our results. We continue the simulations until the interaction region moves out of the grid, until the luminosity becomes about 100 times smaller than at maximum, or when 2 years have passed, whatever comes first.

2.2 Results from the HERACLES simulation

Below, we present the salient features from the interaction simulation, together with illustrations of the bolometric light curve (Fig. 3), the interaction evolution (Figs. 4–7), the properties of the photosphere and of the dense shell (Fig. 8), the evolution of the fluid and of the radiation properties versus radius (Fig. 9), and the shock structure (fig. 10). We define the photosphere as the location where the optical depth integrated inwards from the outer boundary is $2/3$. For convenience, we consider only the electron-scattering opacity when computing the photosphere location. This choice is suitable because the bulk of the emerging radiation emerges in the optical spectral region where electron scattering is the dominant opacity source. At X-ray and UV wavelengths energy-dependent optical depths would need to be used.

Initially the CSM, by construction, is at 2000 K and neutral. It has a huge opacity to Lyman-continuum photons but is transparent at longer wavelengths (Fig. 1). However, after about a week, this CSM is ionised (the ionisation is nearly complete for hydrogen, but only partial for helium). This rapid change occurs as an ionisation front sweeps the CSM (see the early migration of the photosphere, shown as a filled dot, in Fig. 8), triggered by the huge luminosity arising at the shock. At the onset of interaction, both the CSM density and the ejecta velocity are maximum, so the shock luminosity is at its maximum. The luminosity is dominated by the contribution from the forward shock and can be estimated with $L_{\text{shock}} \sim 2\pi r^2 \rho_{\text{CSM}} v_{\text{shock}}^3$ (see, e.g., Chugai & Danziger 1994), which is of the order of $3 \times 10^{44} \text{ erg s}^{-1}$. As time progresses, the fast ejecta is decelerated by the CSM and the shock luminosity decreases. Within 10 d, the maximum velocity is $\sim 6000 \text{ km s}^{-1}$ and the shock luminosity $\sim 3 \times 10^{43} \text{ erg s}^{-1}$. These luminosities are extreme. Adopting a representative radiative luminosity of a few $10^{43} \text{ erg s}^{-1}$ crossing the CSM over the first ten days, this amounts to a total radiative energy on the order of 10^{49} erg , which is 100–1000 times the energy required to ionise the hydrogen atoms in that H-rich shell. Only a small fraction of this energy is absorbed but this is more than sufficient to cause rapid ionisation of the CSM.

Once the CSM is ionised, the minimum continuum opacity is set by electron scattering, and is moderate at all wavelengths. Photons, which are injected at the shock, are thermalised due to the huge X-ray/UV opacity and converted to UV/optical photons. These photons are trapped and escape after diffusing for a time $t_{\text{diff}} \sim \tau_{\text{CSM}} \Delta R/c$, where $\Delta R = R_{\text{phot}} - R_{\text{cds}}$, and R_{phot} is

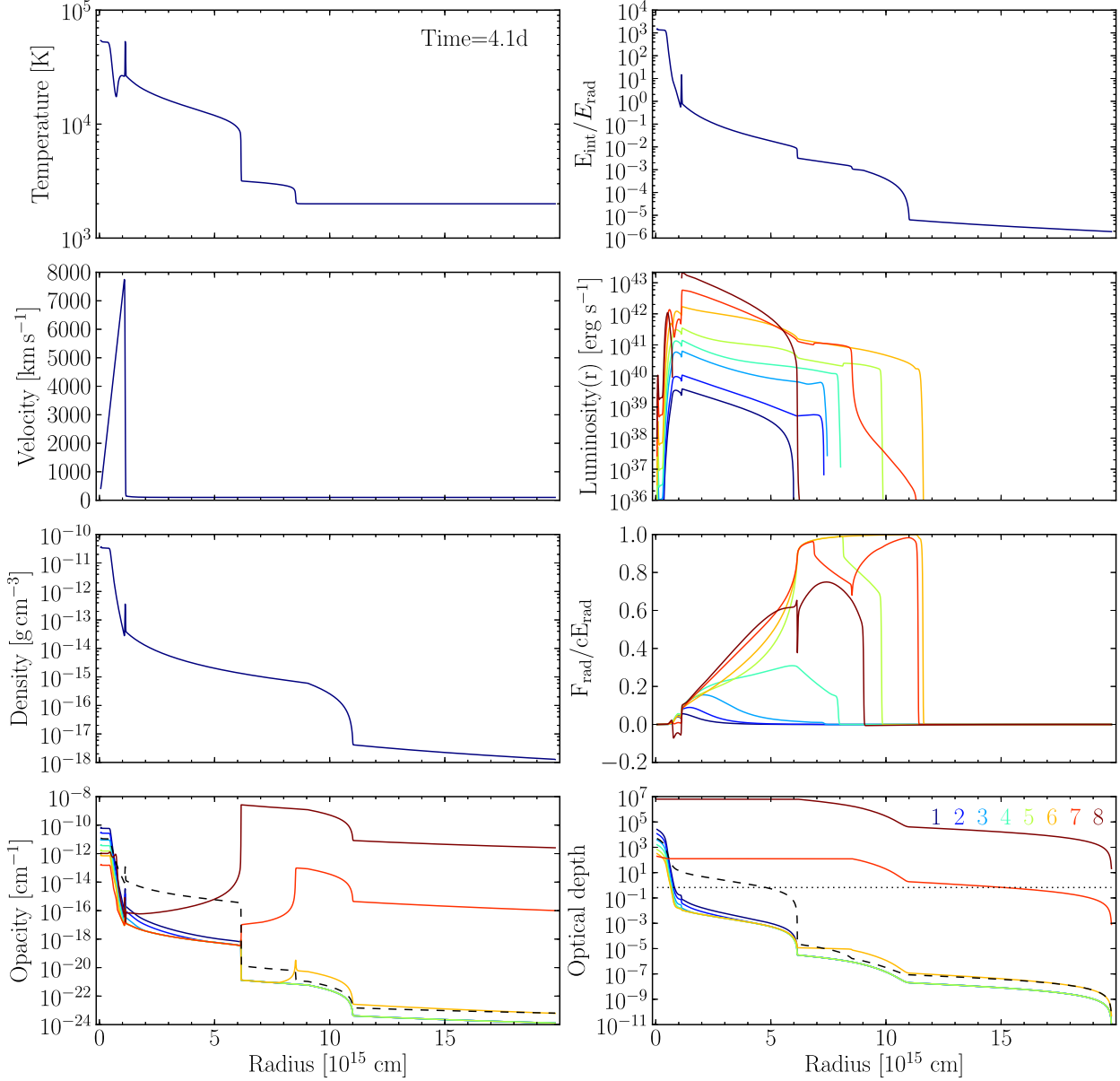


Figure 4. Radial slices through the grid showing the temperature, the ratio of the internal (i.e., gas) energy and the radiation energy (i.e., the mean intensity), the velocity, the luminosity, the mass density, the reduced flux, the opacity (inverse mean free path) for each group (coloured curves) and for electron scattering (dashed black curve) together with the associated optical depth (integrated inwards from the outer boundary; the dotted black line corresponds to $\tau = 2/3$). The coloured curves correspond to each one of the eight energy groups (ordered from low to high energy/frequency; see labels in bottom right panel and discussion in Section 2.1). We use 3 groups longward of the Paschen jump, two groups in the Paschen continuum, two groups in the Balmer continuum, and one group for the Lyman continuum. The time is 4.1 d after the onset of the interaction. The electron scattering contribution is not included in these groups.

the photospheric radius and R_{cds} is the Cold-Dense-Shell (CDS) radius. This CDS is very narrow (i.e., 10^{13} cm) and is bounded by the reverse shock and the forward shock. As can be seen in Figs. 6–7 and Fig. 10, the forward shock exhibits a Zel’dovich spike (Zel’dovich & Raizer 1967) where the gas temperature becomes very high before relaxing to its post-shock value. In practice, the CDS is not cold – its temperature at these early times is in excess of 20000 K, having, however, efficiently cooled from X-ray shock

temperatures by radiative emission.³ In our reference simulation (i.e., for this adopted CSM structure) at 10 days after the onset of

³ We obtain higher spike temperatures of $>10^5$ K with higher resolution. However, it is in practice difficult to resolve the spike structure given the scale of the problem. Shock temperatures of 10^7 – 10^8 K are obtained if we simulate the same interaction configuration without radiation transport (i.e., equivalent to hydrodynamics only). When radiation is included, radiation mediates the properties of the shock. The large heat capacity of the photon gas reduces the shock temperature. The diffusion and the escape of radiation

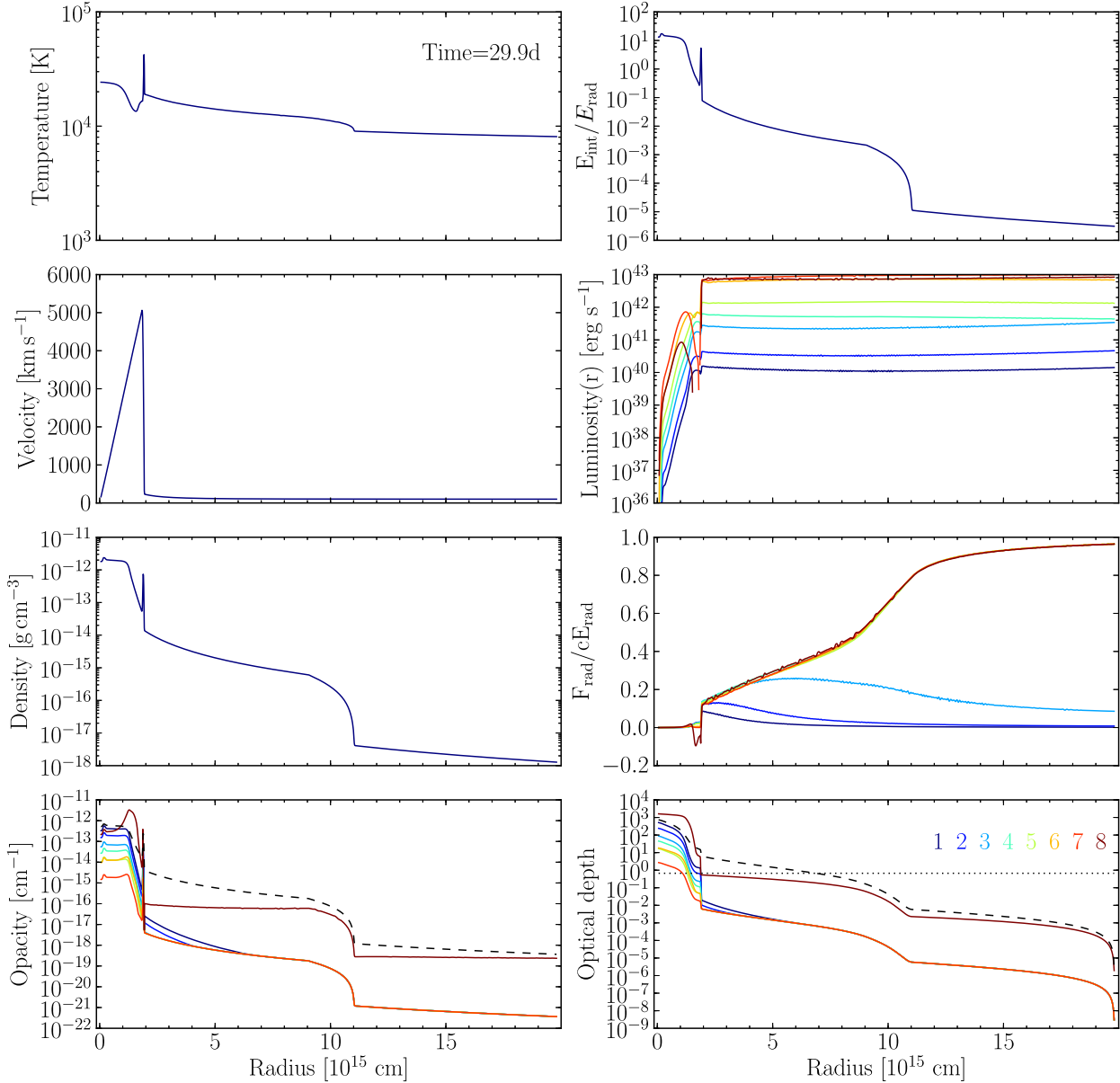


Figure 5. Same as Fig. 4, but now for a time of 29.9 d after the onset of the interaction.

the interaction, $R_{\text{phot}} \sim 7 \times 10^{15}$ cm, the CSM (electron scattering) optical depth is ~ 15 , and the diffusion time from the shock to the photosphere is ~ 35 d.

The light curve we obtain if we assume grey radiation transport (within the M1 model) is quite different (blue curve in Fig. 3), especially at early times. The luminosity is maximum at the beginning, because the grey opacity is very low for cold gas. In contrast, the opacity to X-rays and UV photons is huge at low temperature. Hence, in the grey case, the photons initially produced at the shock travel without being absorbed and reach the outer boundary unadulterated. It is only subsequently that the streaming radiation raises

from the shocked region exacerbates the reduction in temperature of the shocked region compared to a pure hydrodynamics configuration.

the CSM temperature and increases its optical depth, causing a dip and a bump in the light curve, but the corresponding opacity in the X/UV ranges is still much lower than what it is in Nature. The radiation properties (bolometric luminosity, but also colours etc.) are thus affected. This test clearly shows that multi-group radiation transport (with groups that span from short to long wavelength, even coarsely) is important when modelling SNe IIIn.

The evolution of the photospheric radius is quite complicated. Initially it progresses to larger radii as the CSM becomes more ionised. Once the medium is fully ionised, the photospheric radius remains almost constant (Fig. 9). Depending on circumstances, the photospheric radius can then either decrease or increase. First, the CSM may recombine and its opacity to radiation decrease, leading to a recession of the photosphere. This is not seen in our simulations

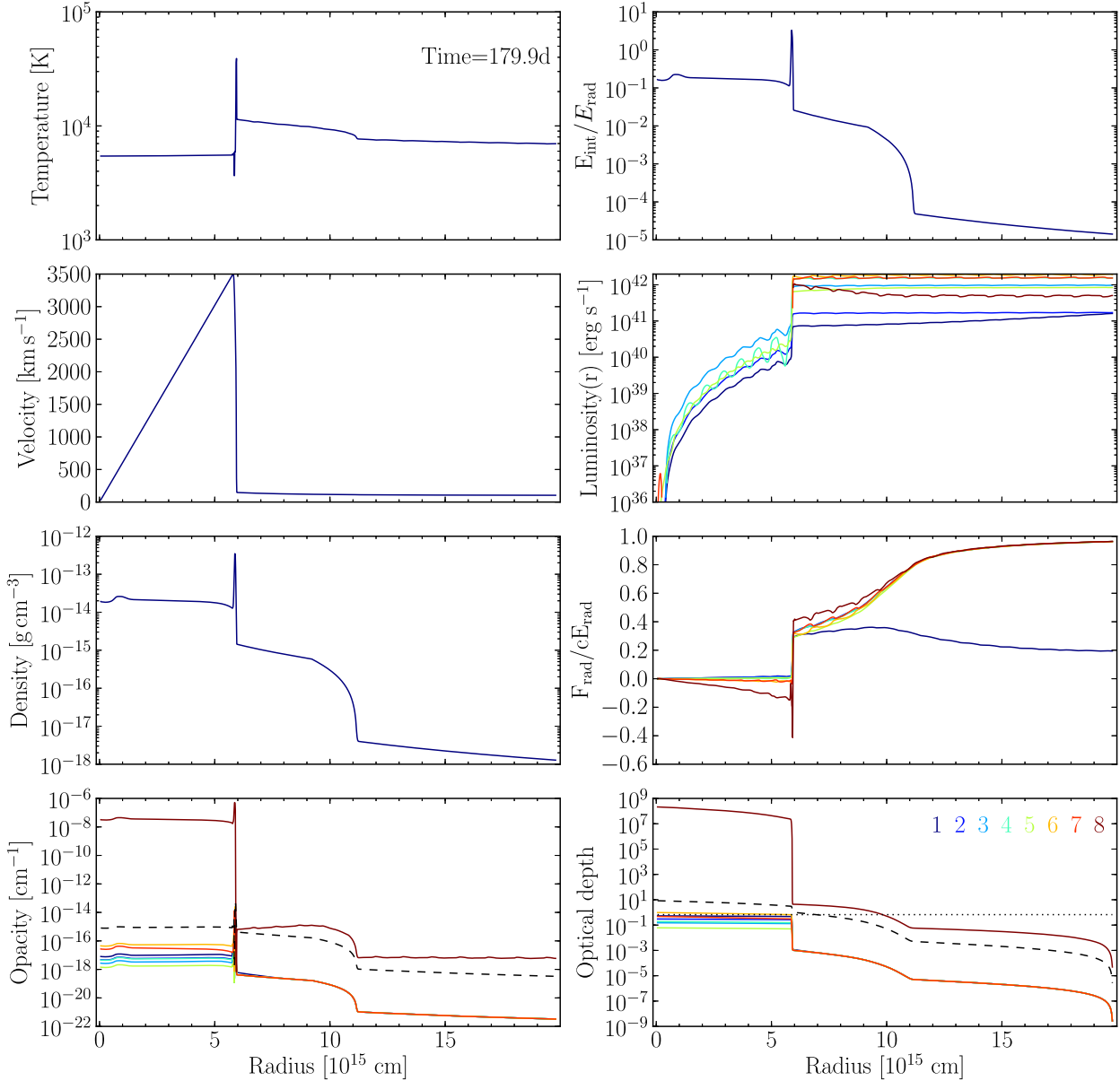


Figure 6. Same as Fig. 4, but now for a time of 179.9 d after the onset of the interaction.

because the large and sustained supply of radiation from the shock maintains a high ionisation in the CSM. The other circumstance, which inevitably occurs, is that the shock (and the CDS), eventually overtakes R_{phot} causing the photospheric radius to increase again. This occurs in this simulation at ~ 200 d, which implies that the average shock velocity over the first 200 days is $\sim 3000 \text{ km s}^{-1}$ (Fig. 8). Because of expansion, the electron-scattering optical depth of the CDS decreases with time.⁴

The evolution of the light curve for the first ~ 200 d is

⁴ This holds once the CSM is fully ionised. Radial compression of CSM material by the shock does not change the CSM electron-scattering optical depth; this would require lateral compression, inexistent in a spherically-symmetric simulation. Absorptive optical depths may increase (because

essentially at fixed R_{phot} . The morphology of the light curve (Fig. 3) differs from the monotonically decreasing shock luminosity because of optical depth effects, very much in the manner of ^{56}Ni powered optically-thick ejecta of standard SNe (Arnett 1982; Chevalier & Irwin 2011; Moriya et al. 2013b). At early times, the L_{shock} is huge but the optical depth is large so radiation energy is stored and released on a diffusion time scale of about a month. Bolometric maximum occurs at $t \sim t_{\text{diff}}$. Past maximum, the SN radiation exceeds for a while and eventually becomes equal to the shock luminosity. A steady-state configuration sets in because the shock luminosity evolves slowly and the diffusion time is only a

such process are often proportional to the square of the density) but except for the optical depth of the Lyman continuum these also decline.

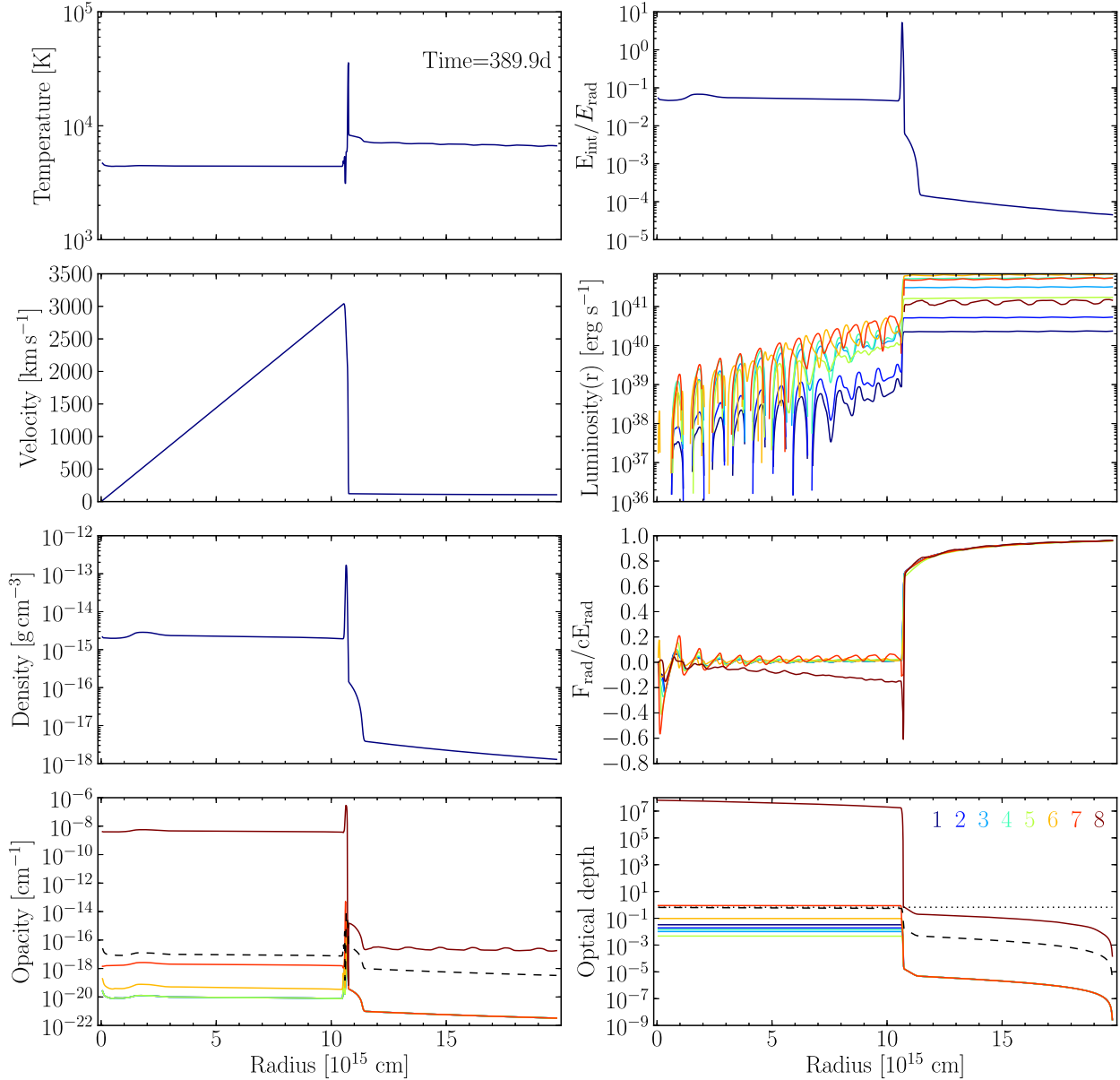


Figure 7. Same as Fig. 4, but now for a time of 389.9 d after the onset of the interaction.

few days (because the CDS gets closer to R_{phot}). Thus, the bolometric evolution over the first 200 d reflects primarily variations not in R_{phot} but in the radiation temperature, itself dependent on the amount of energy injected and stored between the photosphere and the CDS. For times $t < t_{\text{diff}}$, this energy accumulates and the temperature of the optically-thick CSM gas goes up to a maximum around bolometric maximum. For times $t > t_{\text{diff}}$, less and less energy is stored until the steady-state regime is reached. As the shock luminosity decreases, the radiation temperature decreases too and the SN luminosity ebbs.⁵

⁵ In theory, the adopted value of the mean atomic weight should influence the gas temperature. For partial ionisation, the mean atomic weight could be around 0.6-0.7, rather than 1.38, which corresponds to the neutral H-

At the end of the simulation, a total of 0.3×10^{51} erg has been radiated, drawn from the 10^{51} erg of kinetic energy stored in the inner ejecta. There still remains, untapped, 0.7×10^{51} erg of kinetic energy in the system, contained in the un-shocked SN ejecta (i.e., the SN ejecta material not affected by the interaction, which represents 50% of the total SN ejecta mass) and in the massive CDS, which still advances through space at $\sim 3000 \text{ km s}^{-1}$. So, for this configuration, we obtain a conversion efficiency of kinetic to radiation energy of 30% (little additional kinetic energy will be ex-

rich gas adopted here. We ran a simulation for the reference model X with a value of 0.6, but found very similar results, probably because in super-luminous SNe IIn, the entire material is partially ionised throughout most of the evolution — the ionisation state of the plasma does not change.

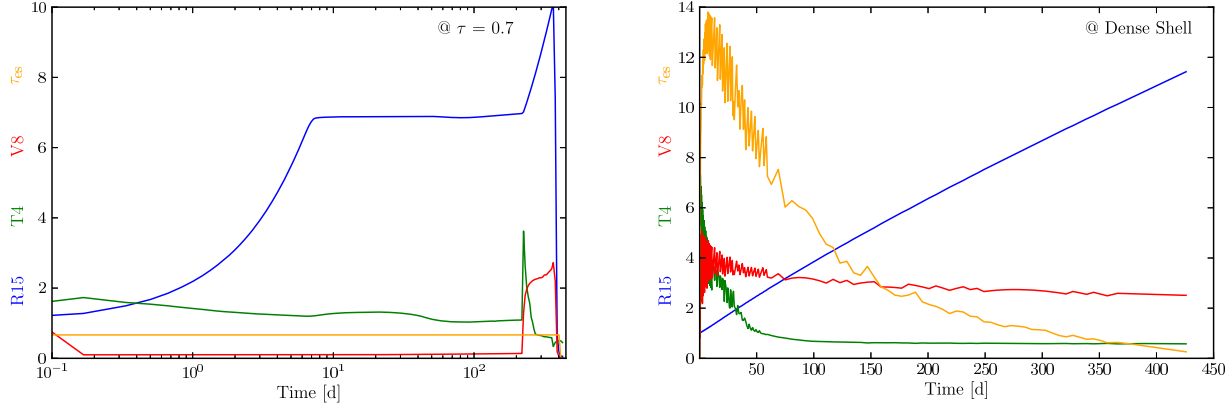


Figure 8. Illustration of the evolution of the material properties at the photosphere (left; logarithmic scale for abscissa), and at the location of maximum density within the dense shell (right). Note the migration of the photosphere to larger radii during the first 8 days, as well as the sudden jump in photospheric properties at ~ 220 d, when the CSM material exterior to the CDS is no longer optically thick (because the CDS has swept up the dense part of the CSM).

tracted in this interaction because the remaining CSM is very low density). In a multi-dimensional configuration, some kinetic energy could also be stored in the lateral direction. Hence, the present 1-D simulation likely overestimates what the equivalent 3-D simulation would produce. Unlike Moriya et al. (2013b), we make no attempt to estimate this, in part because these lateral motions will be much slower than the radial motion of the material and thus cannot represent a large energy loss for the radiation.

In the next section, we will discuss in more detail the radiative transfer properties of this interaction. One thing to note is that despite the significant optical depth of the configuration, the photon mean free path is non negligible. This is particularly true in the inner ejecta region once expansion has caused significant cooling because these regions do not benefit from the shock luminosity (the bulk of the radiation streams radially outwards from the interaction). There is a temperature jump ahead of the interaction (Fig. 10) caused by radiation leakage from the shock, as in the phenomenon of shock breakout in core-collapse SNe (Klein & Chevalier 1978). This structure is comoving with the shock, since the conditions that cause it persist for as long as the shock remains optically-thick.

Our results are in agreement with the radiation hydrodynamics simulations of Moriya et al. (2013b). Our simulation also emphasises that the shell shocked model (Smith & McCray 2007) is not adequate for optically-thick super-luminous SNe IIn, as also pointed out by Moriya et al. (2013a). The basic inconsistency with the shell-shocked model is that it is not possible for a shock to cross a very extended CSM, ionise it, store energy within it, and *subsequently* let this shocked material radiate the deposited energy. This scenario applies to shocks crossing the interior of a stellar envelope (as in successful core-collapse SNe) only because the stellar interior has a huge optical depth. At every location except for the outermost stellar layers, the radiation dominated shock progresses outward faster than the photons it carries in its wake because the photon mean free path is exceedingly small and photon diffusion times exceedingly long compared to the shock-crossing time. In interacting SNe, this configuration does not hold at all. Even for very high CSM densities, the shock-crossing time through the CSM will always far exceed the diffusion time through the shell so that radiation deposited by the shock is *continuously* being radiated by the shocked material. The present simulation shows that the basic light curve properties of super luminous SNe can be explained with a simple and physically consistent setup. It also illustrates how the

simplistic “diffusion model” can be misleading, and how an argument based on dimensional analysis can sometimes lead to wrong conclusions.

In our simulations spectrum formation takes place primarily in the slow moving CSM for about 200 d, but past that the spectrum formation region will be tied to the much faster moving CDS. The CDS optical depth will be too small to ensure full thermalisation within the slow unshocked material even if the location where the optical depth is $2/3$ (i.e., the photosphere), lies there. This implies that line profiles should evolve and become more Doppler-broadened as time passes in super-luminous SNe, while line broadening by electron scattering would dominate only at early times (Dessart et al. 2009). This behaviour is important to study as it carries information on the potentially large residue of kinetic energy left untapped in the interaction. For example, this matters when estimating the kinetic energy in the inner shell and whether this inner shell originates in an energetic explosion that requires the gravitational collapse of the iron core of a massive star.

The radiation injected by the shock and crossing the CSM does work on the material and accelerates it. This radiative acceleration is however modest, and limited to the peak time of the light curve, leading to an increase of the CSM velocity from 100 to ~ 200 km s $^{-1}$ (Fig. 9). At early times, the material that receives a larger acceleration, just ahead of the shock, lies at a large optical depth and is thus less visible than the photons emitted further out, in regions where the acceleration is more modest. At late times, the material ahead of the shock is too optically-thin to receive a significant acceleration. The radiative acceleration in the HERACLES simulation is likely underestimated because of the neglect of line opacity and the potential boost from line desaturation caused by velocity gradients (Castor et al. 1975; Owocki 2015). However, our simulations suggest that the radiation arising at the shock only cause a modest acceleration of the unshocked CSM. This is compatible with the near-constant width of the narrow P-Cygni profile seen in SN 2010jl (Fransson et al. 2014). As we discuss in the next section, this modest acceleration seems an unlikely origin of the peak blueshift seen in the broad emission component of H α .

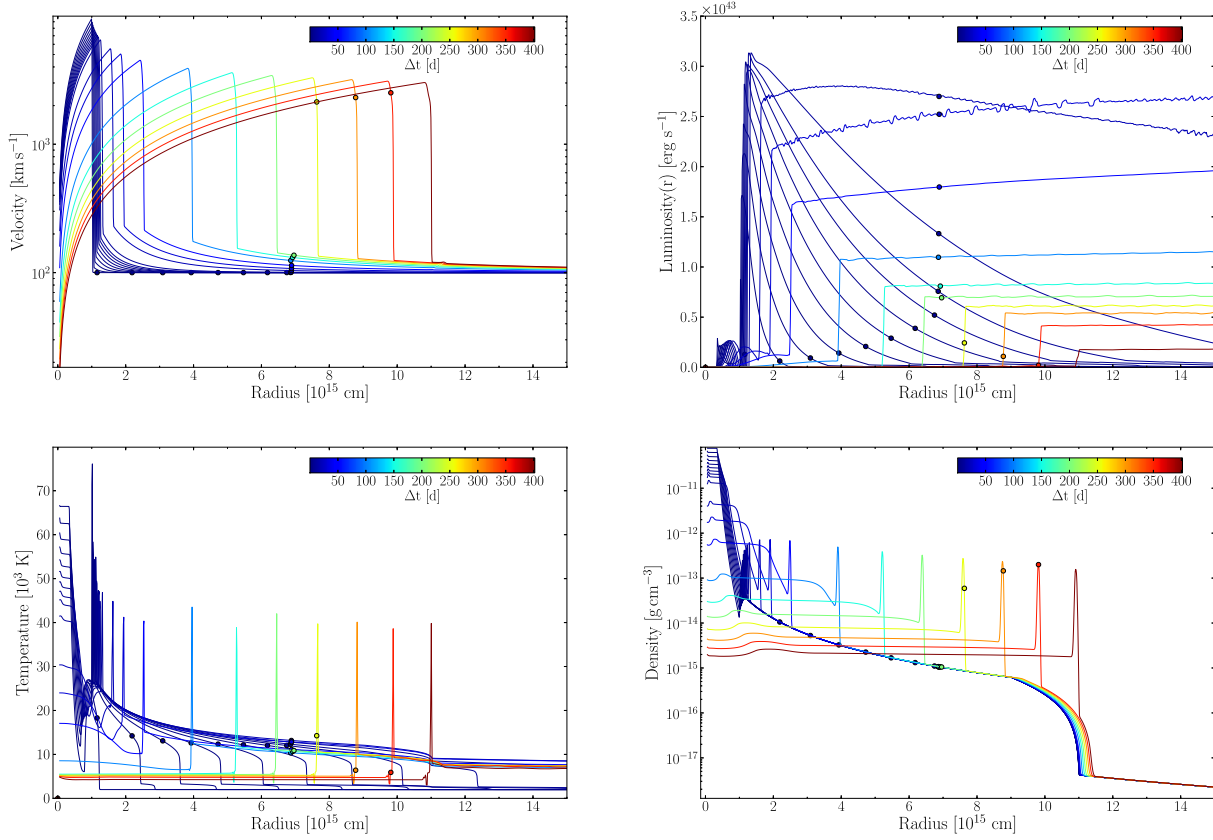


Figure 9. Evolution of the radial profiles for the velocity, luminosity, temperature, and mass density for the reference model X. The epochs shown are 0.01, 1, 2, 3, 4, 5, 6, 7, 8, 10, 20, 30, 50, 100, 150, 200, 250, 300, 350, 400 d after the onset of the interaction. Dots refer to the location of the photosphere — such a location exists for about 350 d, first located in the CSM and then in the CDS. Past 350 d, the total electron scattering optical depth is less than 2/3, making electron scattering a poor frequency-redistribution mechanism at such late times.

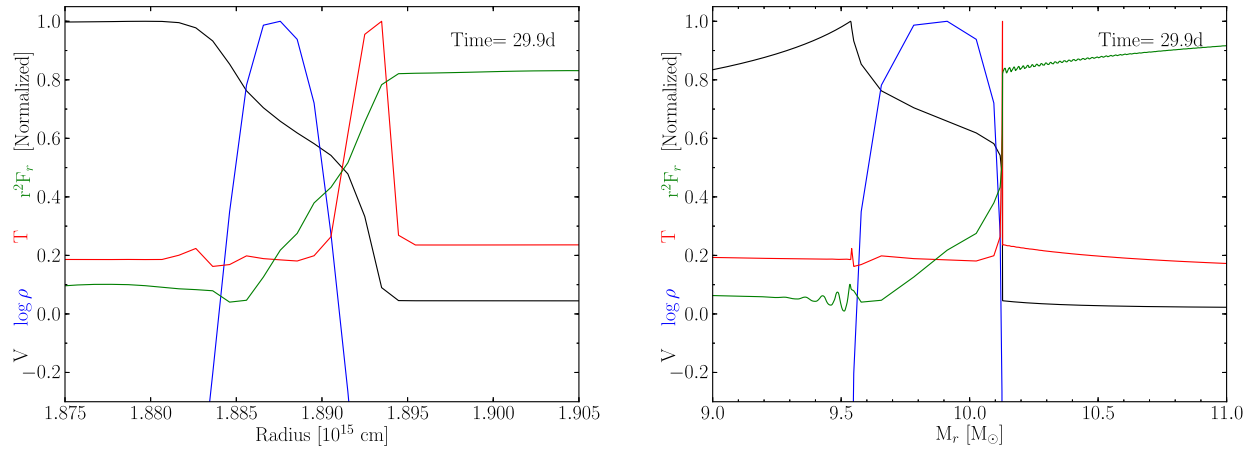


Figure 10. Profiles for the density, temperature, velocity, and bolometric luminosity in the shock region at maximum light (all normalised for visibility) as a function of radius (left) and mass (right) in the reference model X. The resolution is somewhat too small to fully resolve the shock structure, a problem that arises from the Eulerian approach.

3 SPECTROSCOPIC MODELLING WITH CMFGEN

3.1 Numerical approach

At selected epochs during the evolution, from 20 to ~ 200 d after the onset of the interaction, we post-process the HERACLES simulation with the non-LTE radiative transfer code CMFGEN (Hillier & Miller 1998; Hillier & Dessart 2012). While there is no explicit time-dependence in the CMFGEN simulations undertaken here, time dependence is implicitly taken into account since we use the density, temperature, and velocity structures computed with HERACLES. We thus retain a much higher physical consistency than in Dessart et al. (2009). We use an adaptive grid to resolve carefully the strongly varying density and temperature profiles, as well as the optical depth. The grid is truncated at small radii when the inward integrated Rosseland-mean optical depth reaches 30. The final models discussed here use 100 grid points and adopt a turbulent velocity of 20 km s^{-1} .

We use the same H, He, and Fe mass fractions as for the radiation-hydrodynamical simulations. We limit the model atom to H I, He I, He II, Fe I–VI with the same super-level assignment as in Dessart et al. (2013). Higher ionisation stages are unnecessary since the gas temperature in the simulations at the times considered is below $\sim 80000 \text{ K}$ (this maximum temperature is limited to a few zones at the shock and to early times). In the present simulations, the spectrum formation region has a characteristic temperature of about 10000 K or less. A discussion of the signatures of ions from CNO and other intermediate mass elements (which are merely trace elements compared to H and He here) is deferred to a subsequent study.

The current version of CMFGEN does not allow us to calculate non-LTE line blanketed model atmospheres for non-monotonic velocity flows. This property of interacting SNe is however fundamental and should be taken into account. In this work, to overcome this limitation and take into account the non-monotonic velocity structure, we ignore lines when treating the continuous spectrum, but model the lines for the non-LTE analysis using the Sobolev approximation. Non-monotonic velocity flows do not cause major issues with the Sobolev approximation⁶ since it is a local approximation that uses the absolute value of the velocity gradient to compute the optical depth (Castor 1970). Since the density and temperature structures are taken from the hydrodynamical simulation we believe this to be a very reasonable first approach.

To compute the observed spectrum we wrote a new routine capable of computing J in the comoving frame in the presence of non-monotonic velocity fields. With this routine we were able to allow for the influence of (non-coherent) electron scattering which was iterated to convergence using a simple lambda-iteration. Relatively minor changes were then made to CMF_FLUX (Busche & Hillier

2005) to facilitate the computation of the observed spectrum in the observer's frame.

In Dessart et al. (2009), we used a prescription for the density structure of the emitting region and the ansatz was that an optically-thick shell was radiating the flux. In that approach, the entire grid was in radiative equilibrium, and the flux was forced to diffuse through the densest regions of the atmosphere (these regions were also the hottest by imposing the diffusion approximation at the base). The dynamical configuration presented in Section 2 is obviously quite different, but this simplistic treatment is in fact not so bad at early times, when the interaction region and the inner CSM are optically thick because in this case the details of the inner boundary conditions are lost. Hence, for as long as the configuration is optically thick, the approach of Dessart et al. (2009) can provide a good match to the observations of some SNe II_n like 1994W without being dynamically consistent.

3.2 Spectral evolution

We thus compute non-LTE spectra at 20.8, 41.7, 62.5, 83.3, 104.2, 125.0, 145.8, 166.7, 208.3 d after the onset of the interaction. The spectral evolution shown in Fig. 11 reveals a striking similarity to observations of numerous super-luminous SNe II_n, including SN 2010jl (Zhang et al. 2012; Fransson et al. 2014). The SED evolves very slowly with time, with a progression towards redder colours, a diminishing flux shortward of 4000 Å , and a decreasing ionisation visible through the strengthening of Fe II lines. H I and He I lines behave in a more complicated way.

Line profiles prior to 100 days show the distinct symmetric morphology resulting from frequency redistribution by scattering with thermal electrons (Chugai 2001; Dessart et al. 2009), with a typical width of a few 1000 km s^{-1} — in earlier calculations, where we limited the velocities to 100 km s^{-1} on the CMFGEN grid, we obtained similar profiles. The width of this component only reflects redistribution of photons in frequency space by electron scattering — it provides no information about the shock velocity. Superposed on the broad wings, is a very narrow component with a P-Cygni profile morphology. This narrow component corresponds to line emission and absorption weakly affected by electron scattering, and which preferentially arises from the outer regions of the CSM (which are moving at $\gtrsim 100 \text{ km s}^{-1}$ in our model X) where line opacity may still be large but where the electron-scattering opacity is negligible.

At a qualitative level, the early-time spectra shown in Fig. 11 are analogous to those computed in Dessart et al. (2009) despite the very different approaches in the description of the density/temperature structure.

After 100 days, the line profile morphology changes. In addition to the two components discussed above, we see a blue shifted emission component that arises from the CDS. It is blue shifted because the CDS is moving at a velocity of $\sim 3000 \text{ km s}^{-1}$ and is optically thick in the continuum — line photons emitted in the red are absorbed by the near side of the CDS. The blueshift of peak emission seen in non-interacting Type II SNe (Dessart & Hillier 2005b) has a similar origin. These H α properties agree well at the qualitative level with the observations of SN 2010jl (Zhang et al. 2012), although the magnitude of the emission blueshift is overestimated and the magnitude of the line width is underestimated (Fig. 12).

We give a summary of the CMFGEN model properties in Table 2. The CMFGEN bolometric luminosity agrees with the HERACLES value to within 5–25% at early times (i.e. prior to ~ 200 d), which is noteworthy since the two codes differ vastly in the treat-

⁶ One problem we needed to address is that the Sobolev optical depth becomes infinite for one particular direction when the radial velocity gradient is not positive. This occurs because in a spherical flow the Sobolev optical depth is proportional to $1/|1 + \sigma\mu^2|$, where $\sigma \equiv d \ln V / d \ln R - 1$. The angular factor will be infinite when $\mu = \pm 1/\sqrt{-\sigma}$. In practical terms this does not affect the escape probability very much due to the small solid angle subtended by the singularity. However, in the standard computational approach the angle grid is not well sampled (the sampling becomes worse as we move away from $\mu = 1$), and numerical instabilities occurred at one or two depths, which we overcame by limiting the increase in optical depth. In this work we used the simple approach of choosing $\max(|1 + \sigma\mu^2|, -0.2(1 + \sigma))$ for $|1 + \sigma\mu^2|$ when $\sigma < 0$.

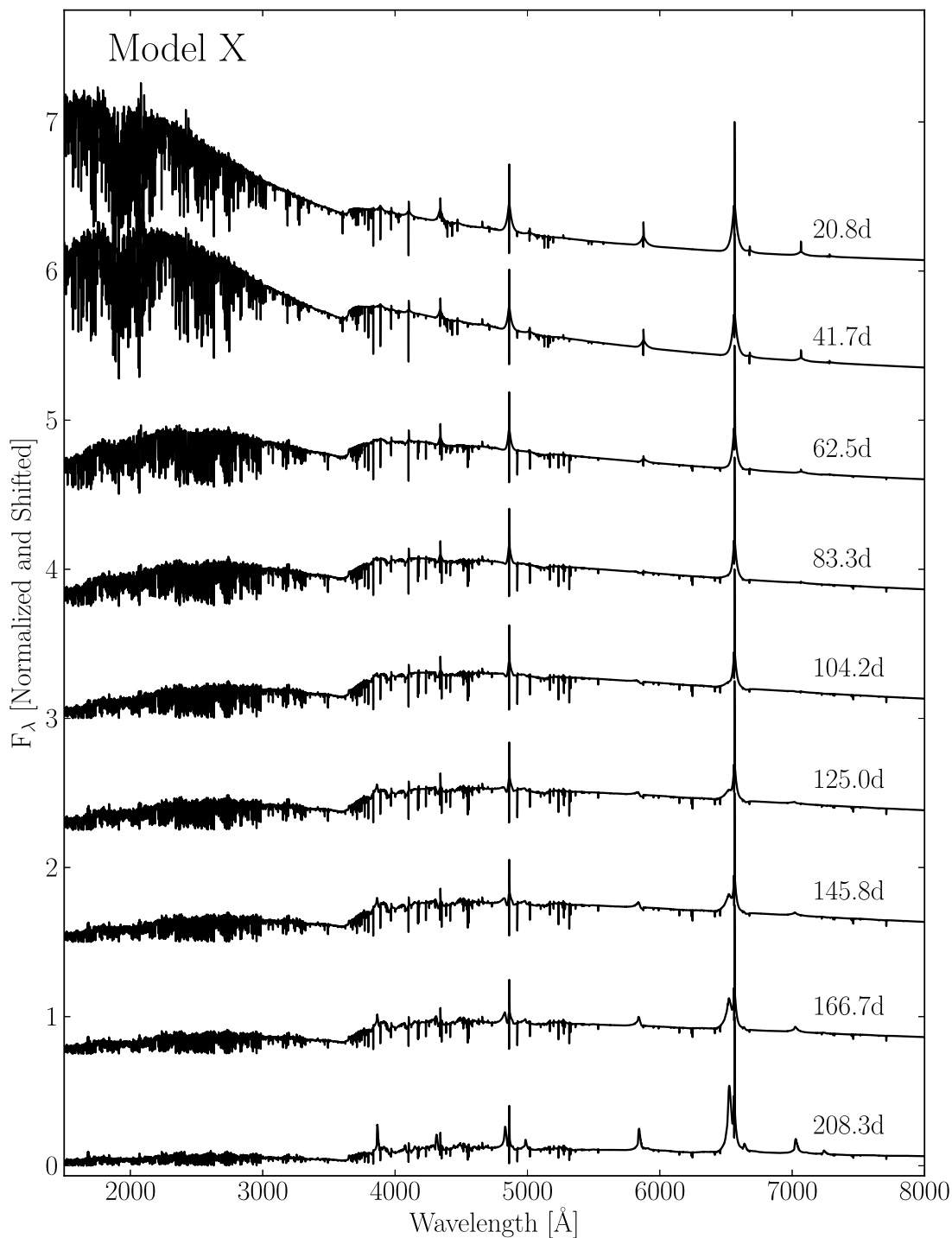


Figure 11. Montage of spectra at selected epochs (see right label) for our reference model X. The high-frequency patterns in the UV are caused by line blanketing from Fe II and Fe III in this model, while the optical is composed of H I, He I, and Fe II lines. At early times, lines typically show a hybrid morphology with a narrow core and extended wings, up to about 2000 km s^{-1} from line centre. These wings are due to incoherent electron scattering. As time progresses, a blue shifted component, associated with emission from the CDS, grows in strength. Line broadening is then caused by electron scattering and expansion.

Table 2. Summary of properties for the CMFGEN simulations based on the reference interaction model X. We include the properties at the photosphere, at the location of maximum density in the interaction region (the CDS), and the properties of the fitted blackbody (see Fig. 13 for an example). We select epochs when the CDS is well below the photosphere, so that the interaction region is optically thick.

age	L_{bol}	M_B	M_V	M_R	M_I	R_{phot}	T_{phot}	$N_{\text{e,phot}}$	R_{cds}	T_{cds}	$N_{\text{e,cds}}$	R_{bb}	T_{bb}	L_{bb}
[d]	[erg s ⁻¹]	[mag]	[mag]	[mag]	[mag]	[10 ¹⁵ cm]	[10 ⁴ K]	[cm ⁻³]	[10 ¹⁵ cm]	[10 ⁴ K]	[cm ⁻³]	[10 ¹⁵ cm]	[10 ⁴ K]	[erg s ⁻¹]
20.8	2.15(43)	-18.61	-18.68	-18.85	-18.86	7.17	1.33	4.36(8)	1.25	1.66	1.76(11)	1.172	1.084	2.259(43)
41.7	2.23(43)	-18.84	-18.98	-19.14	-19.21	7.10	1.27	4.42(8)	1.78	1.18	1.33(11)	1.448	1.033	2.371(43)
62.5	1.21(43)	-18.40	-18.68	-18.90	-19.03	7.02	1.09	4.05(8)	2.86	1.01	1.05(11)	1.616	0.879	1.289(43)
83.3	9.88(42)	-18.16	-18.55	-18.82	-19.01	7.04	1.00	4.00(8)	3.37	0.79	3.93(10)	1.848	0.788	1.050(43)
104.2	8.65(42)	-17.95	-18.43	-18.74	-18.99	7.11	0.97	3.94(8)	3.91	0.76	2.25(10)	2.083	0.715	9.068(42)
125.0	7.99(42)	-17.74	-18.27	-18.62	-18.89	7.08	0.98	3.96(8)	3.64	0.61	9.24(9)	2.199	0.673	8.496(42)
145.8	7.26(42)	-17.56	-18.12	-18.49	-18.77	7.15	1.00	3.90(8)	4.94	0.69	9.51(9)	2.199	0.646	7.503(42)

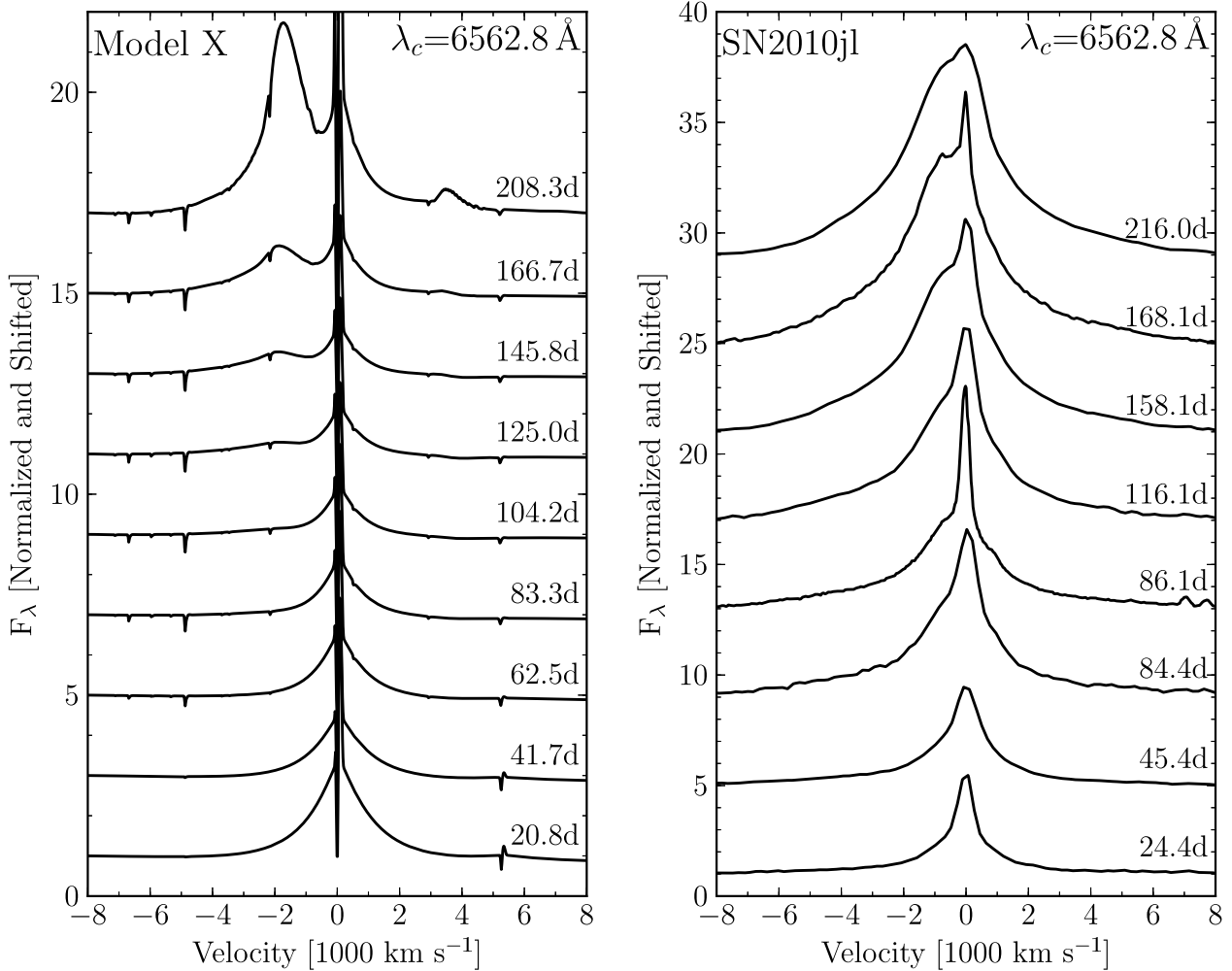


Figure 12. Montage of multi-epoch spectra for Model X (left) and SN2010jl (right; Zhang et al. 2012) shown in velocity space with respect to the rest wavelength of H α . Qualitatively, the model reproduces well the strengthening of the blue-shifted emission component and the increasing width of the observed H α line profile. Quantitatively, the magnitude of the blueshift is somewhat too high while the width of the emission feature is underestimated.

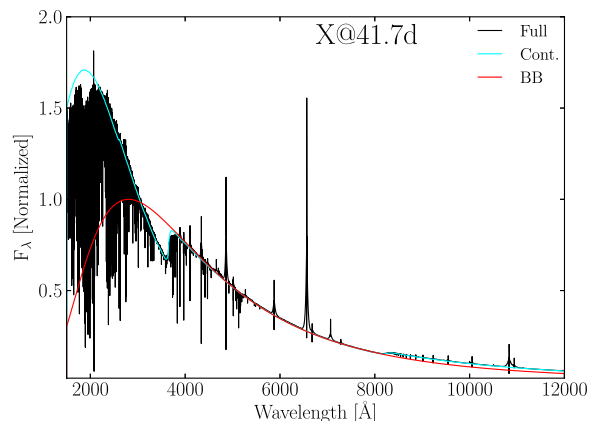


Figure 13. Comparison of the total synthetic flux (black), the continuum synthetic flux (blue) and the best match blackbody flux to the optical range (red), for the reference model X at 41.7 d after the onset of interaction. In the same order, the cumulative luminosities are $5.83 \times 10^9 L_\odot$, $6.18 \times 10^9 L_\odot$, and $4.45 \times 10^9 L_\odot$. The blackbody radius and temperature are 1.45×10^{15} cm and 10331.6 K. The photospheric radius and temperature at that time are 7.10×10^{15} cm and 12670.0 K.

ment of the radiative transfer (M1 method using eight energy groups versus a two-moment solver using 10^5 energy groups) and of the thermodynamic state of the gas (LTE versus non-LTE) — past 200 d, the bolometric luminosity predicted by the two codes differs sizeably (about a factor of 2), probably because non-LTE effects are stronger (the CDS is no longer embedded within the optically thick CSM). A mismatch is expected during the first 1–2 months because light-travel time effects are ignored in the computation of the flux in CMFGEN (the time dependence of the model is implicitly taken into account since we fix the temperature, but no explicit time dependence is accounted for when computing the flux in the formal solution of the radiative transfer equation in CMFGEN). This matters when the properties of the interaction vary on a short time scale (i.e., comparable to the free-flight time of ~ 8 d to the outer boundary, where the luminosity is recorded).

The slow evolution of the SED reflects the slowly varying shock luminosity (which arises from the smooth variation in both the ejecta density/velocity profile and from the slowly varying CSM density for a wind configuration), leading to a decrease in radiation/gas temperature in the optically thick regions of the CSM. Consequently, the electron scattering wings weaken as the ionisation level and the electron scattering optical depth decrease (this is caused by the shrinking of the spectrum formation region, which is bounded by the fixed photosphere and the outward moving dense shell or shock). For about 200 d after the onset of the interaction, the spectrum formation process is essentially unchanged in this simulation.

It is customary in the community to compare the SED with a blackbody. At each epoch, we fit the CMFGEN SED flux ratio between 4800 and 8000 Å to infer T_{bb} — we use an iterative procedure to find the temperature for which the model and the blackbody have between these two wavelengths the same flux ratio to within one part in 10000. We determine the corresponding blackbody radius R_{bb} by matching the blackbody to the model luminosity L_λ at λ (i.e., through $R_{\text{bb}}^2 = L_\lambda / 4\pi^2 B_\lambda(T_{\text{bb}})$). The total blackbody luminosity L_{bb} is then $4\pi R_{\text{bb}}^2 \sigma T_{\text{bb}}^4$. An example is shown in Fig. 13. Although the match is excellent in the fitted range, the SED is not a

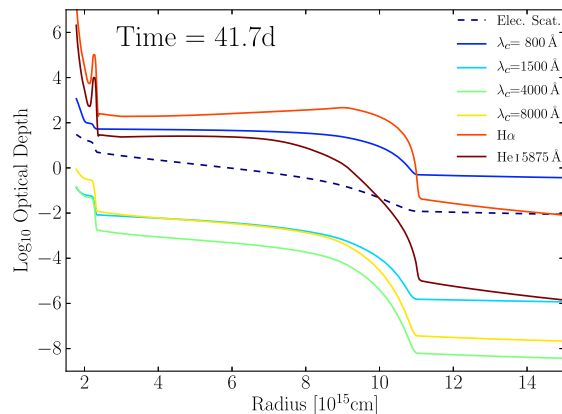


Figure 14. Radial variation of the optical depth associated with electron scattering, various continua, and lines of H α and He I 5875 Å (for which we plot the Sobolev optical depth). Thermalisation in the Lyman continuum is ensured, but not in the Balmer and Paschen continua. The large Sobolev length caused by the small velocity gradient in the CSM causes the H α line optical depth to be very large, and to exceed that in the Lyman continuum.

blackbody. We find non-planckian effects here associated with dilution due to electron scattering (causing $R_{\text{bb}} < R_{\text{phot}}$; see, e.g., Dessart & Hillier 2005a), and flux excess rather than blanketing in the UV (as if multiple blackbody emitters with different temperatures were contributing).

We show the optical depth for electron scattering, selected continuum wavelengths, as well as selected lines in Fig. 14. It is evident that thermalisation is complete for UV photons in this model, but photons redder than the Lyman edge poorly thermalise, even at an early epoch of 41.7 d after the onset of interaction. For these, electron scattering is the main source of opacity. The blackbody radius underestimates the radius of the CDS at all times, although the bulk of the SN flux arises from outside the CDS. Overall, the radiation field in this SN configuration is not well described by the Planck distribution. These considerations are confirmed by Fig. 15, which illustrates how much smaller the mean intensity is compared to the Planck function, except at the location of lines. Furthermore, in our reference model, the bulk of the flux arises at all times from layers where the electron scattering optical depth is never greater than 10, and more typically a few only (see also Fig. 10).

The shallow density structure, the wavelength-dependent opacities, and the strong albedo, lead to a very spatially extended spectrum formation region. For example, the emission/absorption of H α photons occurs throughout the grid, with the exception of the outermost regions of the CSM where the density is very low. At early times observed line photons primarily originate at larger radii because line photons emitted deeper suffer more scatterings, and hence have a greater probability of being absorbed. Line photons that could accrue very large frequency shifts by multiple scattering with thermal electrons tend to be absorbed before they can escape. In our reference model, we find that the bulk of H α photons arise from regions with an electron scattering optical depth of a few, giving rise to emission in line wings extending to ~ 3000 km s $^{-1}$ from line centre, and characterised by a profile with a FWHM of ~ 1500 km s $^{-1}$. This is somewhat similar to values in SN 2010jl (Zhang et al. 2012) at early epochs. However at later times the profiles in SN 2010jl are broader and blue shifted. We also see this

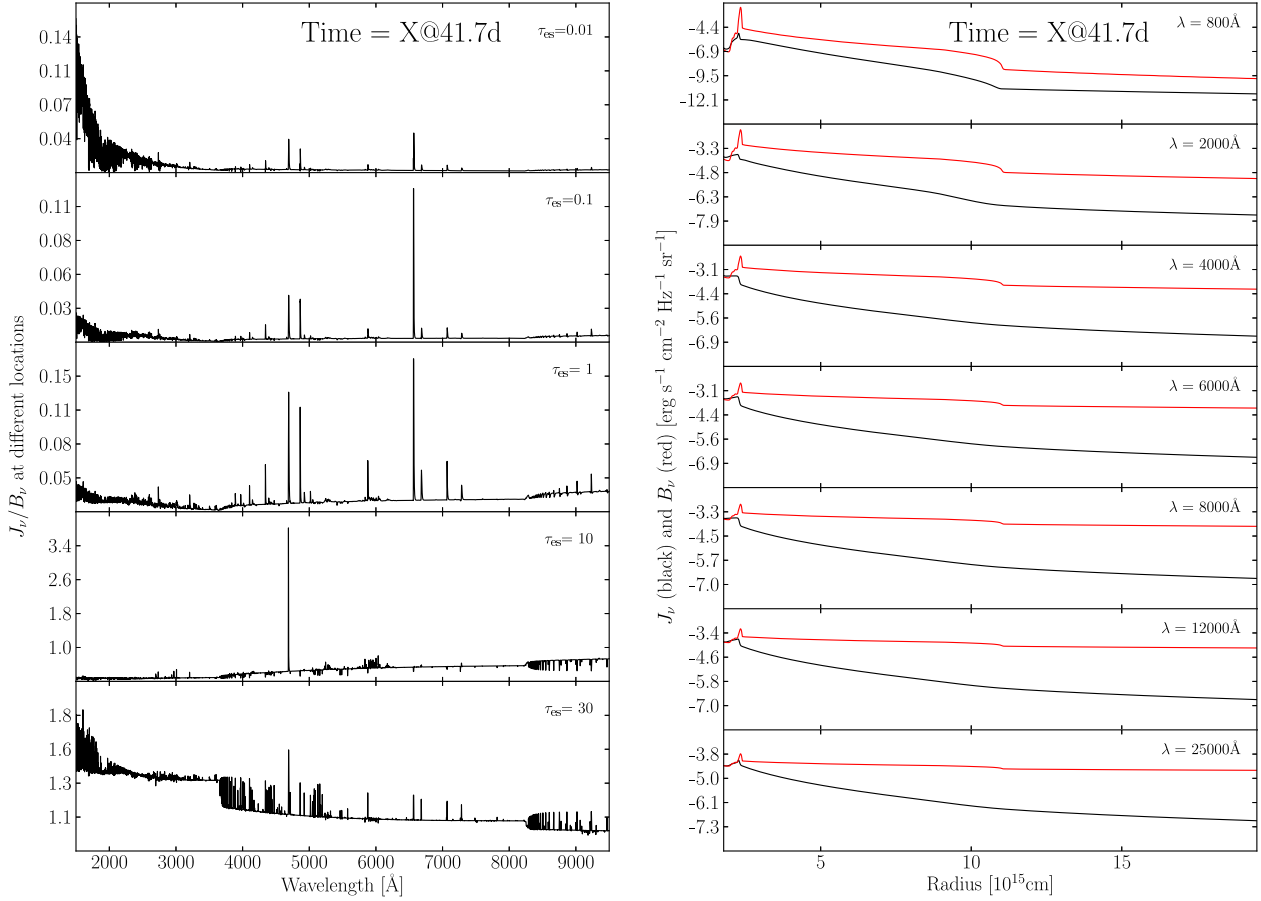


Figure 15. *Left:* Variation of the ratio of the mean intensity J_λ and the Planck function B_λ in the simulation at 41.7 d, shown as a function of wavelength and ejecta/CSM location. The label at right gives the electron-scattering optical depth τ_{es} associated with each panel. At this time, the CDS is at $\tau_{\text{es}} \sim 10$. *Right:* Variation of J_λ and B_λ versus radius and shown for various continuum wavelengths.

effect at late times, with the extra emission associated with the CDS (Fig. 12). The blueshift of the broad $\text{H}\alpha$ line is caused by an optical depth effect that affects all SNe (Dessart & Hillier 2005b; Anderson et al. 2014). At early times, the peak blueshift is not seen because the $\text{H}\alpha$ photons emitted from the CDS are unable to escape – they undergo numerous electron scatterings and are eventually destroyed by a continuum absorption. All these properties are illustrated in Figs. 16–17.

As found in earlier studies (e.g., Hillier 1991) the adopted turbulent velocity also affects the strength of the electron scattering wings. This occurs since a larger turbulent velocity increases the Sobolev length, and hence leads to an increased probability that a line photon scattering within the Sobolev resonance zone will experience an electron scattering interaction, which, because of the large Doppler shift, will cause it to be shifted out of resonance allowing it to escape.

4 POLARISATION CALCULATIONS

The dense shell that forms in the interaction is Rayleigh-Taylor unstable and should be simulated in 3-D — this is left for future work. There is, however, observational evidence from spectropolarimetric observations that some SNe II are asymmetric on large

scale (Leonard et al. 2000; Wang et al. 2001; Hoffman et al. 2008; Patat et al. 2011). This we try to address in this section by performing 2-D polarisation calculations.

We post-process the CMFGEN simulation for model X at 41.7 d by computing linear polarisation profiles in the same fashion as described in Dessart & Hillier (2011). We break spherical symmetry by enforcing a latitudinal variation in density (thus preserving axial symmetry). In practice, we use $\rho(r, \mu) = \rho(r, \mu = 0)(1 + A_1 \mu^2)$, where $\mu \equiv \cos \theta$, and θ is the colatitude. The magnitude of the asymmetry is controlled through the parameter A_1 , which we vary from 0.1, to 0.2, 0.4, 0.8, and 1.6. The resulting axially symmetric ejecta has therefore a prolate morphology, with pole-to-equator density ratios (at a given radius) of 1.1, 1.2, 1.4, 1.8, and 2.6. This adopted type of asymmetry is chosen for its simplicity – other choices might also yield similar continuum and line polarisations.

We show the flux in the $\text{H}\alpha$ line and in the overlapping continuum in Fig. 18 for an observer along a line-of-sight perpendicular to the axis of symmetry. Along this direction, the continuum polarisation has its maximum value, reaching about 1.6% for $A_1 = 1.6$. As we progress towards the $\text{H}\alpha$ rest wavelength from continuum regions (i.e., $\gtrsim 3000 \text{ km s}^{-1}$ from line centre), the polarisation decreases steadily, as observed in SN 2010jl (Patat et al. 2011; Williams et al. 2014) and in some Wolf-Rayet

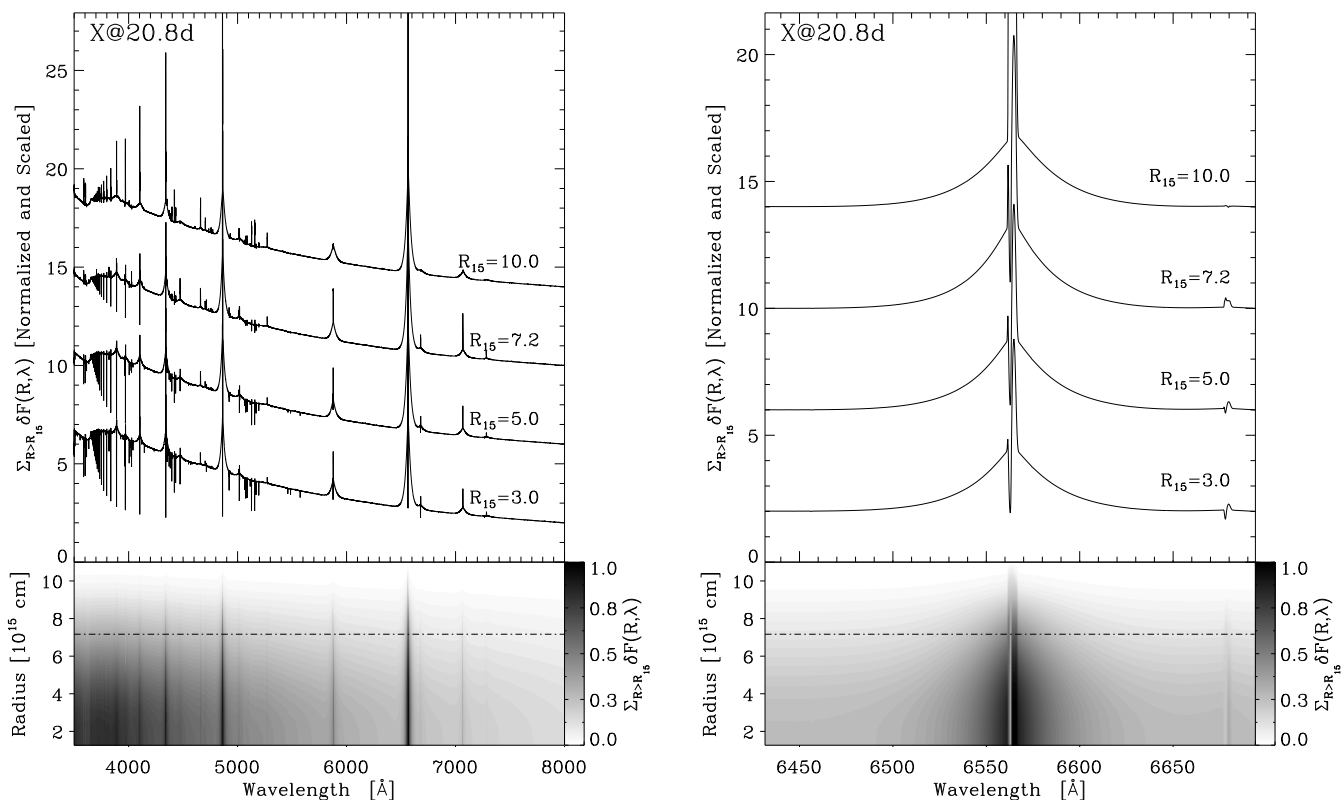


Figure 16. *left:* Illustration of the wavelength (λ) and depth (R) dependence of the quantity $\sum_{R>R_{15}} \delta F(R, \lambda)$, where $\delta F(R, \lambda) = (2\pi/D^2) \int_{\Delta R} \Delta z \eta(p, z, \lambda) e^{-\tau(p, z, \lambda)} p dp$, and R_{15} is R in units of 10^{15} cm. Here, D is the distance; ΔR and Δz are the shell thickness in the radial direction and along the ray with impact parameter p , respectively; $\eta(p, z, \lambda)$ and $\tau(p, z, \lambda)$ are the emissivity and the ray optical depth at location (p, z) and wavelength λ . The gray scale in the bottom panel shows how $\sum_{R>R_{15}} \delta F(R, \lambda)$ varies as we progress inwards from the outer boundary, indicating the relative flux contributions of different regions. If we choose R_{15} as the minimum radius on the CMFGEN grid, we recover the total flux. The grayscale also shows how lines increasingly broaden (and the peak line flux decreases) as we progress outwards. The dash-dotted line corresponds to the radius of the electron-scattering photosphere, and the dashed line (which overlaps with x-abcissa here) corresponds to the CDS radius. The top panel shows selected cuts (see right label) of the quantity $\sum_{R>R_{15}} \delta F(R, \lambda)$. From top to bottom ($R_{15} = 10, 7.2, 5.0, 3.0$), $\sum_{R>R_{15}} \delta F(R, \lambda)$ represents 4, 45, 77, and 98 per cent of the total emergent flux at 6800 \AA . *Right:* Same as left, but now zooming in on the $H\alpha$ region. The depth variation of the line width, influenced by electron scattering, is evident in the bottom panel.

stars (Schulte-Ladbeck et al. 1991; Harries et al. 1998). In our simulation, this reduced polarisation across the line is a signature of the distinct formation of the continuum and the line. Because of the lower optical depth, continuum photon arise from a much greater electron-scattering optical depth than do $H\alpha$ line photons (Fig. 14). Furthermore, line photons emitted in a recombination process start off with zero polarisation, and therefore can only accumulate a lower polarisation through a reduced number of scatterings before escape. This depolarisation is maximum within 100 km s^{-1} of line centre since over this spectral range, one sees photons that underwent essentially no scattering with free electrons (photons scattered by free electrons receive a wavelength-shift and, statistically, end up somewhere in the wings; see discussion in Dessart et al. 2009). In this context, whatever the imposed deformation on the ejecta, the polarisation at line centre is zero.⁷

Surprisingly the polarisation is parallel to the major axis (i.e., positive; see top panel of Fig. 18) — this property is, naively, not

expected since scattering of the light from a point source by an optically thin prolate spheroid has the polarisation at right angles to the major axis (Brown & McLean 1977). In our convention (and that of Brown & McLean 1977), the polarisation is positive when it is parallel to the axis of symmetry (for further details, see Section 2 of Dessart & Hillier 2011). The reason for this behaviour in the current simulation is that the CSM is optically thick, and the observed (and hence scattered) flux predominantly escapes from equatorial regions, where the densities are lowest (Fig 19).

The correspondence between our simulations and the morphology of the polarised and of the total fluxes of SN 2010jl suggests first that our model for super-luminous SNe II In like 2010jl is adequate. Secondly, the observed polarisation implies that the ionised CSM causing the polarisation is significantly asymmetric. If axially symmetric, a pole to equator density ratio of ~ 3 could explain the observed continuum polarisation. While the CSM is asymmetric, it is however unclear whether the inner shell is also asymmetric — it does not need to be. Multi-dimensional radiation hydrodynamics simulations are needed to model the spatial properties of the shocked CSM (for example, in the current context, the shock strength should also be latitude dependent, causing variations in temperature, ionisation, velocities etc with angle), so that we can

⁷ Equivalent simulations for Type II SNe may yield a residual polarisation at line centre because these photons are emitted at a non negligible electron-scattering optical depth (Dessart & Hillier 2011). Spectrum formation in SNe II-P and SNe II In is drastically different.

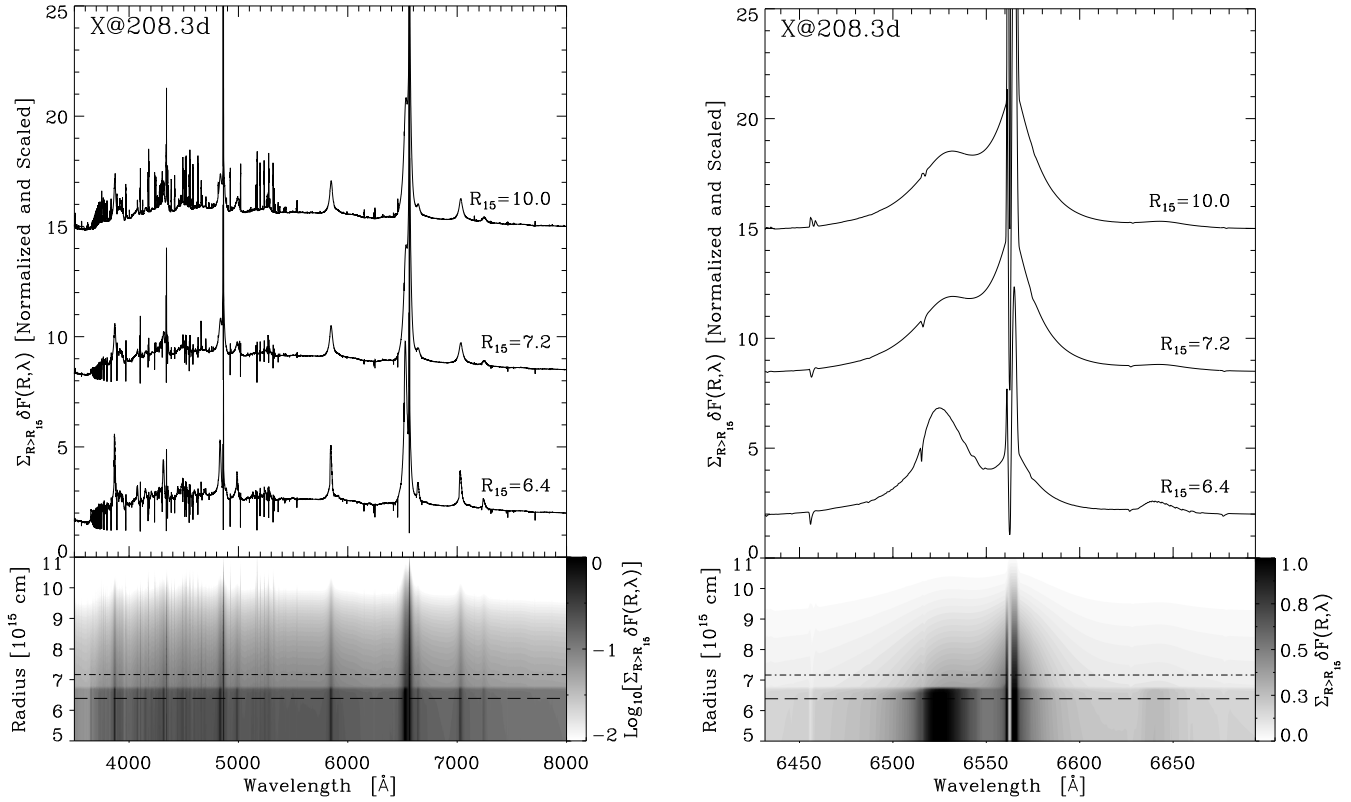


Figure 17. Same as Fig. 16, but now for a time of 208.3 d after the onset of interaction. In the left column, the greyscale is shown on a logarithmic scale. From top to bottom ($R_{15} = 10, 7.2, 6.4$), $\sum_{R>R_{15}} \delta F(R, \lambda)$ represents 6, 41, and 94 per cent of the total emergent flux at 6800 Å. The flux contributions from the fast moving CDS and the slow moving CSM are clearly visible. The emission from the CDS is blue shifted, while the CSM emission is symmetric around line centre. Electron scattering affects the emitted photons from both components.

better characterise the nature of the asymmetry at the origin of the observed polarisation in SNe IIn like 2010jl.

5 DEPENDENCY ON SOME MODEL PARAMETERS

Varying the properties of either the CSM mass or the explosion energy can affect the emergent radiation. This has been discussed in the past for the bolometric luminosity or the colours (see, e.g., Chugai et al. 2004; Woosley et al. 2007; van Marle et al. 2010; Moriya et al. 2013b). Here, we repeat such explorations to investigate the impact on spectral signatures as well.

5.1 Impact on the bolometric light curve

Taking model X as a reference, we produce models in which the SN ejecta kinetic energy is scaled by a factor of 3 (Xe3) or 10 (Xe10). We produce models in which the CSM density is scaled by a factor of 3 (Xm3) or 6 (Xm6). We also consider combinations of both, with models Xe3m6 or Xe10m6. Finally, we consider model Xe3m6r, where the high-density CSM extends to 1.5×10^{16} cm rather than 10^{16} cm only. Table 1 summarises these model properties.

These alterations produce a considerable diversity of bolometric light curves (Fig. 20), in directions that are well understood. Increasing the kinetic energy causes a much greater shock luminosity at all times, but since the CSM structure is not changed, the diffusion time through the CSM is unchanged (the time to maximum is decreased by just a few days for higher SN ejecta kinetic energy).

The bolometric light curves shift upward for increasing energy. The mean radiation-energy density in the CSM also increases with shock luminosity, which raises the radiation temperature. Colours are thus strongly affected, getting bluer for higher energy (see below and Table 1 where we give the bolometric correction and the colour $V - I$ at bolometric maximum).

Varying the CSM mass (corresponding in our approach to a change in mass loss rate) modulates the impedance of the “interaction engine”. For larger CSM density and total mass, more kinetic energy is extracted from the SN ejecta. This energy is converted primarily into radiation. Consequently, varying the CSM mass affects the light curve properties. Higher CSM mass implies higher CSM optical depth and a longer diffusion time, hence a delayed time of peak. A larger CSM mass buffer implies more kinetic energy is tapped so the bolometric maximum is more luminous. In the model set X, Xm3, Xm6, the total energy radiated is 0.32, 0.49, and 0.63×10^{51} erg (for the same ejecta kinetic energy of 10^{51} erg), so, the conversion efficiency can be considerably enhanced when the CSM mass exceeds significantly the SN ejecta mass, with values here as high as $\sim 70\%$ (models Xe3m6, Xe10m6, or Xm6).

Combinations of higher CSM mass and higher ejecta kinetic energy (e.g., model Xe3m6) shift the reference model (quite suitable to SN 2010jl) to the domain where SN 2006gy lies (Smith et al. 2007), with peak luminosities of the order of a few 10^{44} erg s $^{-1}$ sustained for 2–3 months and a peak time that occurs later (~ 2 months after the onset of the interaction).

Finally, extending the region of high density in the CSM from 10^{16} to 1.5×10^{16} cm (models Xe3m6r versus model Xe3m6) leads

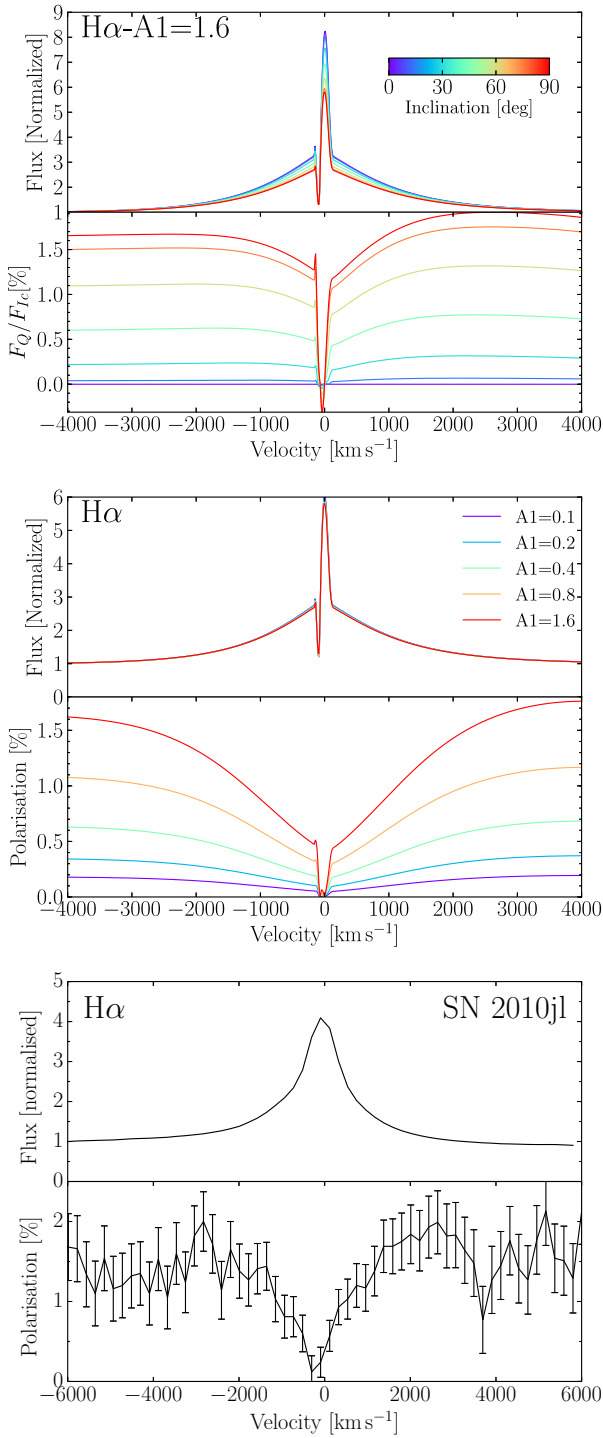


Figure 18. *Top:* Total and polarised flux across the H α line and the overlapping continuum for different inclinations (90° corresponds to an equatorial view), at 41.7 d after the onset of the interaction (hence close to the epoch of maximum light), showing the larger continuum polarisation, the depolarisation across the line profile, and the unpolarised line core. The prolate asymmetry is characterised by a pole-to-equator density ratio of 2.6 ($A_1 = 1.6$). *Middle:* Same as top, but now showing the percentage polarisation for different magnitudes of the asymmetry (A_1 values between 0.1 and 0.6) and for an equatorial view. *Bottom:* Spectro-polarimetric observations of the H α line for SN 2010jl on November 18.2UT (Patat et al. 2011), which is within a few days of our model time (left panel). In the context of our model, the observed polarisation may be interpreted as arising from a prolate CSM with a pole-to-equator density ratio of ~ 3 .

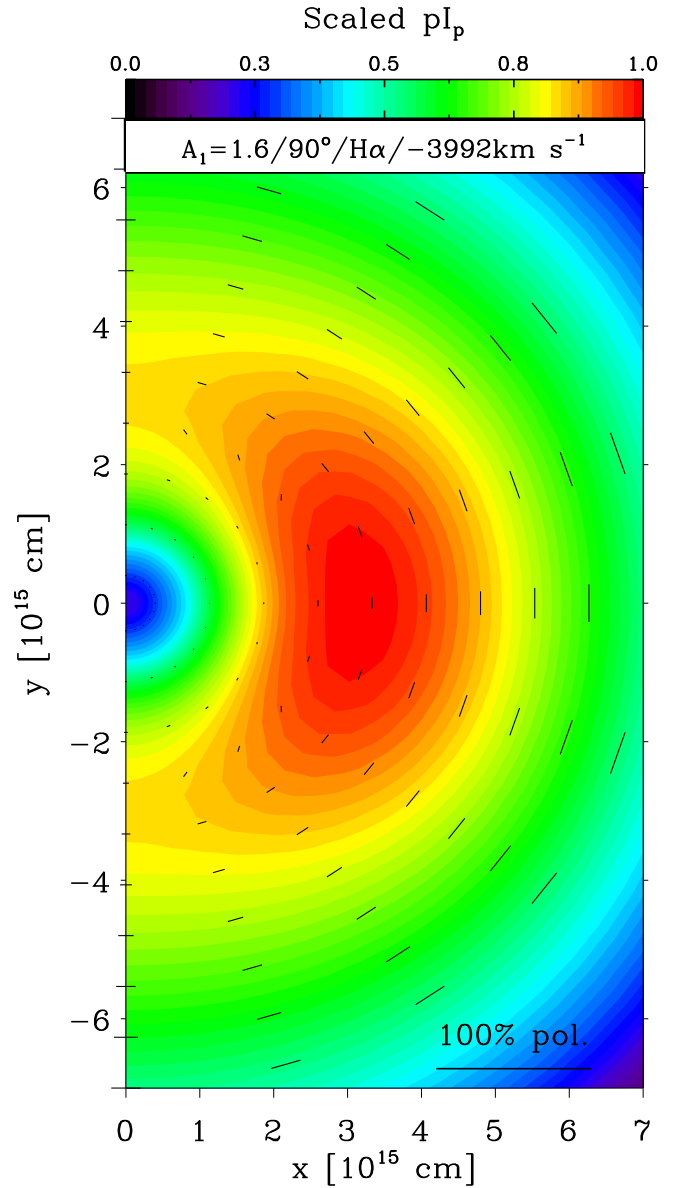


Figure 19. Colour map of the specific intensity (scaled by the impact parameter p) on the plane of the sky at -3992 km s^{-1} from the H α line centre (this Doppler velocity corresponds to a continuum region — see top panel of Fig. 18), for the model with $A_1 = 1.6$, at 41.7 d after the onset of the interaction, and seen at a 90° inclination (i.e. edge-on). We overplot segments (black bars) showing the local polarisation strength and orientation (the length corresponding to 100 per cent polarisation is shown at the bottom right).

to a sustained high luminosity beyond 300 d. In fact, all the light curves in Fig 20 show a break after 150-300 d, except for model Xe3m6r. This light curve break in our simulations is associated with the shock (or the CDS) reaching the outer edge of the denser parts of the CSM (the shock in model Xe3m6r has not yet reached $1.5 \times 10^{16} \text{ cm}$ at the last time shown in Fig. 20) and starting to encounter lower density material (see Table 1 for details).

The pre-acceleration of the CSM by the radiation from the shock depends on the adopted configuration. In model X, we obtained a modest enhancement in CSM velocity from 100 to 200 km s^{-1} . This pre-acceleration is stronger when we use a larger ejecta kinetic energy (stronger shock, higher luminosity) or if the

CSM density is increased (there is a delicate balance to get here since a higher CSM density means a higher opacity and thus more radiation momentum extracted but it also implies more inertia) — see Fig. 21.

5.2 Impact on maximum light spectra

The diversity in bolometric light curves discussed in the preceding section is also strongly present in the spectra at maximum light (Fig. 22). For the highest energy explosion, the shift in temperature in the ionised CSM leads to a major rise in ionisation for hydrogen and helium, producing very blue and nearly featureless spectra (whatever blanketing from Fe occurs in the UV and far-UV). For models with enhanced CSM mass, the temperature/ionisation conditions are comparable to reference model X, but the line fluxes are increased. The higher the CSM mass, the redder the colour at peak.

Interestingly, in models with very high CSM mass, although the Balmer line fluxes are much higher, the extent of the electron scattering wings does not increase beyond a maximum of $\sim 3000 \text{ km s}^{-1}$. The likely reason is that line photons do not just scatter off free electrons in the CSM — there is a non-zero probability that they are absorbed in a bound-free or free-free process leading to photon destruction. The broader and blue shifted lines seen at late times require that we see photons blue shifted by expansion. For the present case, the broader blue-shifted component seen at late times arises from the CDS. We see a blue-shift since the CDS absorbs emission from the far side of the shell. Thus the $H\alpha$ blueshift seen in SN 2010jl (Smith et al. 2012; Zhang et al. 2012; Fransson et al. 2014) might simply just stem from an optical-depth effect, without any dust intervening in the process. As the optical depth of the shell declines, we expect the profile to become more symmetric.

6 CONCLUSION

In this work, we have presented numerical simulations for interacting SNe in which both the kinetic energy of the explosively-produced inner shell and the mass of the wind-produced outer shell are very large. We used an inner shell kinetic energy of 10^{51} erg or more, and a CSM mass of at least $3 M_{\odot}$. These simulations correspond to possible configurations for super-luminous SNe IIn.

Our contribution is novel because we post-process our multi-group radiation-hydrodynamics simulations with radiative transfer tools, to compute non-LTE spectra and polarisation signatures. With this more global approach, we can study the numerous features that make super-luminous SNe IIn unique.

We find that the light curve of a super-luminous SN IIn is composed of several distinct phases. Initially, the cold CSM is neutral and transparent to optical photons. As the interaction starts, the radiation from the shock drives an ionisation front through the CSM and makes it optically thick at all wavelengths. This first phase takes about a week after the onset of the interaction, which corresponds roughly to the light crossing time through the shell. At the time we record the first emerging photons from the SN IIn, the CSM is therefore already optically thick. In our reference model, the photosphere is then located at $\sim 7 \times 10^{15} \text{ cm}$ and will remain at that radius for months. The second phase corresponds to the shock crossing of the optically thick CSM. In our reference model, this phase lasts $\gtrsim 200 \text{ d}$. Over this duration, the shock is located below the photosphere, at an electron-scattering optical depth of about 15 initially. Radiation from the shock is thus continuously released

deep in the CSM and comes out on a diffusion time scale. This context is analogous to optically thick ejecta influenced by radioactive decay, although the shock energy is not all channeled into radiation energy. Here, the shock luminosity decreases with time because of the decreasing shock strength as more and more CSM is being swept up. Although the CSM hardly expands, the diffusion time scale and the optical depth decrease because of the expansion of the interaction region. We thus obtain a bell shape morphology for the light curve around maximum. This variation is not associated by the migration of the photospheric radius, but by the variation in shock luminosity, radiation temperature, and CSM/photospheric temperature. Optical depth effects on the light curve persist for as long as the shock is located below the $\sim 7 \times 10^{15} \text{ cm}$. The third phase starts when the shock overtakes this location. The photosphere then follows the dense shell.

Our multi-group radiation hydrodynamics simulation produces the basic light curve morphology of type IIn super-luminous SNe. Our reference model was tuned to roughly match the inferred properties of SN 2010jl (Fransson et al. 2014), but other simulations with different inner-shell kinetic energy and CSM mass encompass a variety of light curves, including extreme events like SN 2006gy (Smith et al. 2007).

We illustrate the importance of performing *multi-group* radiation hydrodynamics. By contrast, *grey* (i.e., one-group) radiation hydrodynamics simulations do not account adequately for the opacity of the material and produce a discrepant SN IIn light curve morphology.

Our simulations confirm the earlier work of Moriya et al. (2013b) that the shell shocked model of Smith & McCray (2007) is not physically sound. The reason is that in interacting SNe, even a massive CSM cannot have a continuum optical depth greater than a few tens. Because such CSM are by nature extended, the shock-crossing time far exceeds the time it takes the shock luminosity to diffuse through the optically thick layers. The situation is analogous to shock emergence in an exploding star, except that here the configuration is quasi steady state — it persists for as long as there is optically-thick CSM material ahead of the shock. Our results, which are in agreement with the independent simulations of Moriya et al. (2013b), provide a simple and physically consistent explanation for the light curves of type IIn super-luminous SNe. Overall, the shell-shocked model really belongs to the domain of (successful) core-collapse SNe in which a radiation-dominated shock crosses a stellar envelope whose optical depth is huge everywhere apart from the surface.

The non-LTE radiative transfer simulations, based on the radiation hydrodynamics simulations, produce spectra that are initially blue and redden progressively as the CSM/photosphere cools down after bolometric maximum. We obtain symmetric emission profiles, broadened by non-coherent scattering with free electrons (of thermal origin), with wings that extend up to 3000 km s^{-1} from line centre, and together with a narrower P-Cygni profile ($< 100 \text{ km s}^{-1}$) forming in the outer cold CSM. Varying the ejecta kinetic energy or the CSM mass alters the shock luminosity, the mean radiation energy in the optically thick CSM, and causes clear variations in colour and ionisation. Varying the CSM density by a factor of 6 changes the strength of recombination lines but does not produce broader lines at bolometric maximum, despite the enhanced electron-scattering optical depth. Photons emitted at an optical depth τ perform τ^2 scatterings before escaping. If the albedo is 99%, photons coming from $\tau > 10$ are likely absorbed within the ionised CSM and photons do not obtain arbitrarily large frequency

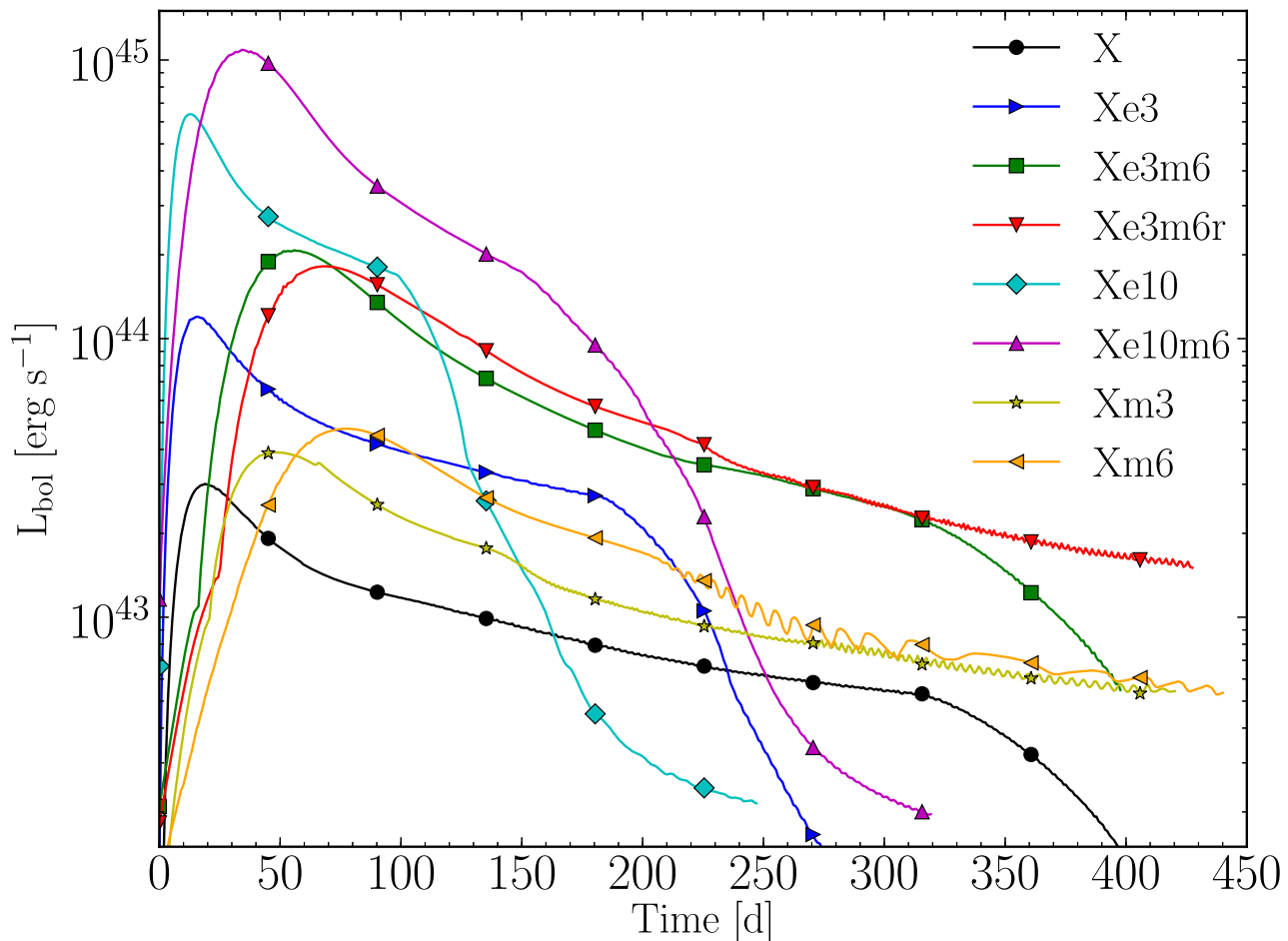


Figure 20. Light curve diversity obtained by varying some of the parameters of our reference model X (see details in Table 1). Models whose name contains en have a SN ejecta kinetic energy scaled by a factor n relative to model X. Models whose name contains mn have a CSM mass loss rate scaled by a factor n relative to model X. Model Xe3m6r differs from the rest because the dense part of the CSM extends to 1.5×10^{16} cm rather than 10^{16} cm.

shifts from line centre. Broader electron scattering wings may arise for a greater albedo.

Our simulations indicate that photon absorption is probably efficient only in the Lyman continuum. At low photon frequencies, absorptive processes are weak and therefore photon absorption occurs only if the total optical depth at the site of emission is large (say above 10) — in our reference simulation with a mass loss rate of $0.1 M_{\odot} \text{ yr}^{-1}$ for the CSM, the maximum CSM continuum τ is only 15. Early on, the optical depth in the CDS is high enough to ensure complete thermalisation. Then, line broadening is probably dominated by non-coherent scattering with thermal electrons. However, at later times, thermalisation does not occur at all depths in the CSM. In the reference model, this is associated with an increased broadening and blueward asymmetry of line profiles with time. These features are also present in the observations of SN 2010jl (e.g., $H\alpha$; Fig. 12) — this suggests a growing contribution from Doppler broadening, connected with photon emission from the fast expanding CDS. We believe this hybrid line formation is at the origin of the very large $H\alpha$ line width in SN 2010jl, as well as the blueshift of its peak emission. Interestingly, the modest peak luminosities and the absence of broad lines at all times

in events like SN 1994W (Chugai et al. 2004; Dessart et al. 2009) or SN 2011ht (Humphreys et al. 2012) are perplexing because the emission from the CDS should be seen once the CSM becomes transparent.

To complement our radiation hydrodynamics simulations with HERACLES and our non-LTE radiative transfer simulations with CMFGEN, which assume spherical symmetry, we present some polarisation simulations for aspherical but axially symmetric configurations. Our results for a prolate morphology with a pole-to-equator density ratio of ~ 3 yield a maximum $\lesssim 2\%$ continuum polarisation compatible with the value observed for SN 2010jl (Patat et al. 2011). In this context, the asymmetry may stem only from the CSM, although both inner and outer shells may be asymmetric. In future work, we will extend the HERACLES simulations to 2-D to study large scale asymmetries and to 3-D to study the stability of the dense shell.

ACKNOWLEDGMENTS

We thank Ralph Sutherland and Claes Fransson for discussion and comments, and Nando Patat for providing the spectropolari-

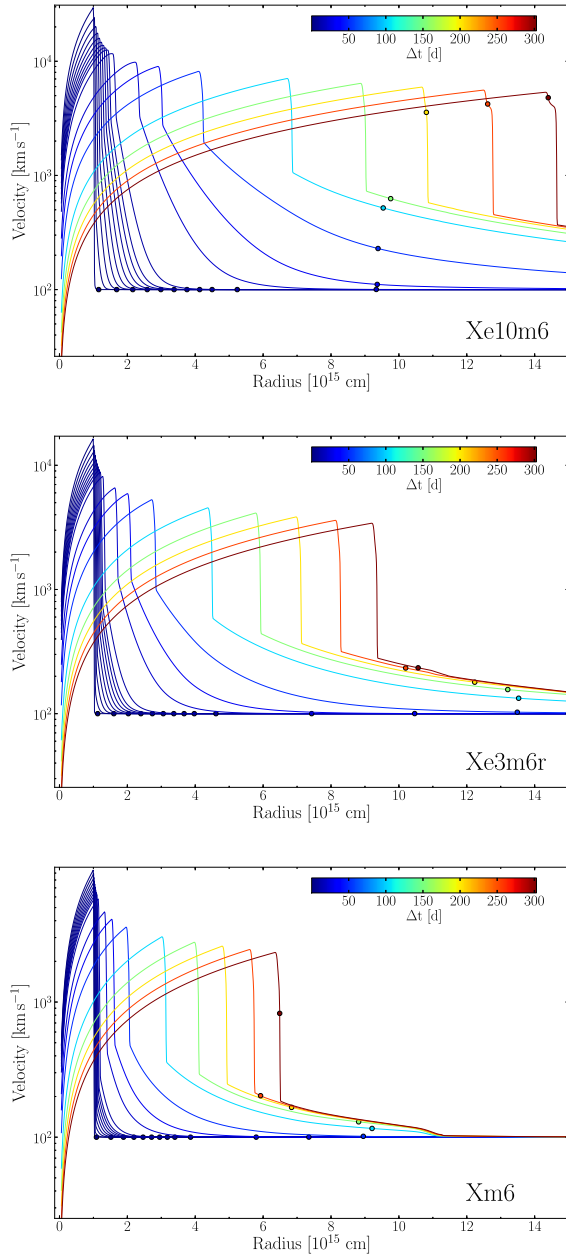


Figure 21. Velocity profiles from the HERACLES simulations for models Xe10m6 (top), Xe3m6r (middle), and Xm6 (bottom). The epochs shown correspond to 0.01, 1, 2, 3, 4, 5, 6, 7, 8, 10, 20, 30, 50, 100, 150, 200, 250, and 300 d after the onset of the interaction. Notice the pre-acceleration that takes place ahead of the shock.

metric data for SN2010jl published in Patat et al. (2011). Dessart acknowledges financial support from the European Community through an International Re-integration Grant, under grant number PIRG04-GA-2008-239184, and from “Agence Nationale de la Recherche” grant ANR-2011-Blanc-SIMI-BS56-0007. Hillier acknowledges support from STScI theory grant HST-AR-12640.01, and NASA theory grant NNX10AC80G. This material is based upon work partially supported by the National Science Foundation under grant number AST-1311993. Hillier would also like to acknowledge the hospitality and support of the Distinguished Visitor program at the Research School of Astronomy and Astrophysics

(RSAA) at the Australian National University (ANU). This work was also supported in part by the National Science Foundation under Grant No. PHYS-1066293 and benefited from the hospitality of the Aspen Center for Physics. This work was granted access to the HPC resources of CINES under the allocations c2013046608 and c2014046608 made by GENCI (Grand Equipement National de Calcul Intensif). This work also utilised computing resources of the Mésocentre SIGAMM, hosted by the Observatoire de la Côte d’Azur, Nice, France.

REFERENCES

- Anderson, J. P., Dessart, L., Gutierrez, C. P., Hamuy, M., Morrell, N. I., Phillips, M., Folatelli, G., Stritzinger, M. D., Freedman, W. L., González-Gaitán, S., McCarthy, P., Suntzeff, N., & Thomas-Osip, J. 2014, *MNRAS*, 441, 671
- Arnett, W. D. 1982, *ApJ*, 253, 785
- Barkat, Z., Rakavy, G., & Sack, N. 1967, *Physical Review Letters*, 18, 379
- Blondin, J. M., Lundqvist, P., & Chevalier, R. A. 1996, *ApJ*, 472, 257
- Brown, J. C. & McLean, I. S. 1977, *A&A*, 57, 141
- Busche, J. R. & Hillier, D. J. 2005, *AJ*, 129, 454
- Castor, J. I. 1970, *MNRAS*, 149, 111
- Castor, J. I., Abbott, D. C., & Klein, R. I. 1975, *ApJ*, 195, 157
- Chen, K.-J., Woosley, S., Heger, A., Almgren, A., & Whalen, D. J. 2014, *ApJ*, 792, 28
- Chevalier, R. A. & Irwin, C. M. 2011, *ApJL*, 729, L6
- Chugai, N. N. 2001, *MNRAS*, 326, 1448
- Chugai, N. N., Blinnikov, S. I., Cumming, R. J., Lundqvist, P., Bragaglia, A., Filippenko, A. V., Leonard, D. C., Matheson, T., & Sollerman, J. 2004, *MNRAS*, 352, 1213
- Chugai, N. N. & Danziger, I. J. 1994, *MNRAS*, 268, 173
- Dessart, L. & Hillier, D. J. 2005a, *A&A*, 439, 671
- . 2005b, *A&A*, 437, 667
- . 2011, *MNRAS*, 415, 3497
- Dessart, L., Hillier, D. J., Gezari, S., Basa, S., & Matheson, T. 2009, *MNRAS*, 394, 21
- Dessart, L., Hillier, D. J., Waldman, R., & Livne, E. 2013, *MNRAS*, 433, 1745
- Dessart, L., Livne, E., & Waldman, R. 2010a, *MNRAS*, 408, 827
- . 2010b, *MNRAS*, 405, 2113
- Dopita, M. A., Cohen, M., Schwartz, R. D., & Evans, R. 1984, *ApJL*, 287, L69
- Dubroca, B. & Feugeas, J. 1999, *CRAS*, 329, 915
- Fransson, C., Ergon, M., Challis, P. J., Chevalier, R. A., France, K., Kirshner, R. P., Marion, G. H., Milisavljevic, D., Smith, N., Bufano, F., Friedman, A. S., Kangas, T., Larsson, J., Mattila, S., Benetti, S., Chornock, R., Czekala, I., Soderberg, A., & Sollerman, J. 2014, *ApJ*, 797, 118
- González, M., Audit, E., & Huynh, P. 2007, *A&A*, 464, 429
- Grasberg, E. K. & Nadezhin, D. K. 1986, *Soviet Astronomy Letters*, 12, 68
- Harries, T. J., Hillier, D. J., & Howarth, I. D. 1998, *MNRAS*, 296, 1072
- Hillier, D. J. 1991, *A&A*, 247, 455
- Hillier, D. J. & Dessart, L. 2012, *MNRAS*, 424, 252
- Hillier, D. J. & Miller, D. L. 1998, *ApJ*, 496, 407
- Hoffman, J. L., Leonard, D. C., Chornock, R., Filippenko, A. V., Barth, A. J., & Matheson, T. 2008, *ApJ*, 688, 1186
- Humphreys, R. M., Davidson, K., Jones, T. J., Pogge, R. W.,

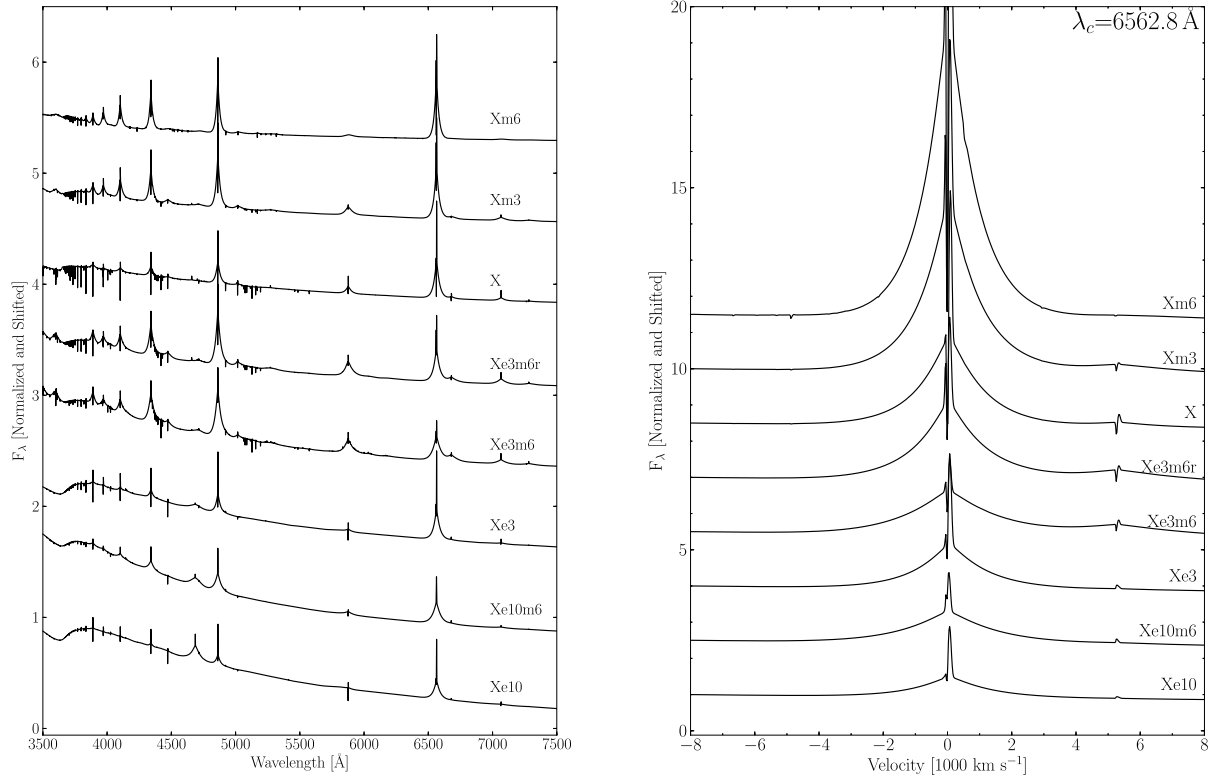


Figure 22. *Left:* Maximum light spectra for the interaction models with different ejecta kinetic energy and/or CSM mass/density (see Table 1 for additional details). Note the strong shift in colour for interaction models with higher ejecta kinetic energy. *Right:* Same as left, but showing the H α line region, in velocity space. Interestingly, even for very large CSM densities (and thus mass loss rates), the maximum extent of the electron-scattering wings is 2000-3000 km s⁻¹. The much broader wings of H α in SN 2010jl as time progresses suggest that they do not stem exclusively from scattering with electrons but must instead contain a contribution from Doppler-shifted line photons (i.e., emitted from the fast moving material in the interaction region).

Grammer, S. H., Prieto, J. L., & Pritchard, T. A. 2012, *ApJ*, 760, 93

Klein, R. I. & Chevalier, R. A. 1978, *ApJL*, 223, L109

Leonard, D. C., Filippenko, A. V., Barth, A. J., & Matheson, T. 2000, *ApJ*, 536, 239

Margutti, R., Milisavljevic, D., Soderberg, A. M., Chornock, R., Zauderer, B. A., Murase, K., Guidorzi, C., Sanders, N. E., Kuin, P., Fransson, C., Levesque, E. M., Chandra, P., Berger, E., Bianco, F. B., Brown, P. J., Challis, P., Chatzopoulos, E., Cheung, C. C., Choi, C., Chomiuk, L., Chugai, N., Contreras, C., Drout, M. R., Fesen, R., Foley, R. J., Fong, W., Friedman, A. S., Gall, C., Gehrels, N., Hjorth, J., Hsiao, E., Kirshner, R., Im, M., Leloudas, G., Lunnan, R., Marion, G. H., Martin, J., Morrell, N., Neugent, K. F., Omodei, N., Phillips, M. M., Rest, A., Silverman, J. M., Strader, J., Stritzinger, M. D., Szalai, T., Uterback, N. B., Vinko, J., Wheeler, J. C., Arnett, D., Campana, S., Chevalier, R., Ginsburg, A., Kamble, A., Roming, P. W. A., Pritchard, T., & Stringfellow, G. 2014, *ApJ*, 780, 21

Mauerhan, J. C., Smith, N., Filippenko, A. V., Blanchard, K. B., Blanchard, P. K., Casper, C. F. E., Cenko, S. B., Clubb, K. I., Cohen, D. P., Fuller, K. L., Li, G. Z., & Silverman, J. M. 2013, *MNRAS*, 430, 1801

Moriya, T. J., Blinnikov, S. I., Baklanov, P. V., Sorokina, E. I., & Dolgov, A. D. 2013a, *MNRAS*, 430, 1402

Moriya, T. J., Blinnikov, S. I., Tominaga, N., Yoshida, N., Tanaka, M., Maeda, K., & Nomoto, K. 2013b, *MNRAS*, 428, 1020

Niemela, V. S., Ruiz, M. T., & Phillips, M. M. 1985, *ApJ*, 289, 52

Ofek, E. O., Zoglauer, A., Boggs, S. E., Barrière, N. M., Reynolds, S. P., Fryer, C. L., Harrison, F. A., Cenko, S. B., Kulkarni, S. R., Gal-Yam, A., Arcavi, I., Bellm, E., Bloom, J. S., Christensen, F., Craig, W. W., Even, W., Filippenko, A. V., Grefenstette, B., Hailey, C. J., Laher, R., Madsen, K., Nakar, E., Nugent, P. E., Stern, D., Sullivan, M., Surace, J., & Zhang, W. W. 2014, *ApJ*, 781, 42

Owocki, S. P. 2015, in *Astrophysics and Space Science Library*, Vol. 412, *Astrophysics and Space Science Library*, ed. J. S. Vink, 113

Owocki, S. P., Gayley, K. G., & Shaviv, N. J. 2004, *ApJ*, 616, 525

Pastorello, A., Cappellaro, E., Inserra, C., Smartt, S. J., Pignata, G., Benetti, S., Valenti, S., Fraser, M., Takáts, K., Benitez, S., Botticella, M. T., Brimacombe, J., Bufano, F., Cellier-Holzem, F., Costado, M. T., Cupani, G., Curtis, I., Elias-Rosa, N., Ergon, M., Fynbo, J. P. U., Hamsch, F.-J., Hamuy, M., Harutyunyan, A., Ivarson, K. M., Kankare, E., Martin, J. C., Kotak, R., LaCluyze, A. P., Maguire, K., Mattila, S., Maza, J., McCrum, M., Miluzio, M., Norgaard-Nielsen, H. U., Nysewander, M. C., Ochner, P., Pan, Y.-C., Pumo, M. L., Reichart, D. E., Tan, T. G., Taubenberger, S., Tomasella, L., Turatto, M., & Wright, D. 2013, *ApJ*, 767, 1

Patat, F., Taubenberger, S., Benetti, S., Pastorello, A., & Harutyunyan, A. 2011, *A&A*, 527, L6

Schlegel, E. M. 1990, *MNRAS*, 244, 269

- Schulte-Ladbeck, R. E., Nordsieck, K. H., Taylor, M., Nook, M. A., Bjorkman, K. S., Magalhaes, A. M., & Anderson, C. M. 1991, *ApJ*, 382, 301
- Smith, N., Li, W., Foley, R. J., Wheeler, J. C., & et al. 2007, *ApJ*, 666, 1116
- Smith, N. & McCray, R. 2007, *ApJL*, 671, L17
- Smith, N., Silverman, J. M., Filippenko, A. V., Cooper, M. C., Matheson, T., Bian, F., Weiner, B. J., & Comerford, J. M. 2012, *AJ*, 143, 17
- Sollerman, J., Cumming, R. J., & Lundqvist, P. 1998, *ApJ*, 493, 933
- Stathakis, R. A. & Sadler, E. M. 1991, *MNRAS*, 250, 786
- Stoll, R., Prieto, J. L., Stanek, K. Z., Pogge, R. W., Szczygieł, D. M., Pojmański, G., Antognini, J., & Yan, H. 2011, *ApJ*, 730, 34
- Turatto, M., Cappellaro, E., Danziger, I. J., Benetti, S., Gouiffes, C., & della Valle, M. 1993, *MNRAS*, 262, 128
- van Marle, A. J., Smith, N., Owocki, S. P., & van Veelen, B. 2010, *MNRAS*, 407, 2305
- Vaytet, N. M. H., Audit, E., Dubroca, B., & Delahaye, F. 2011, *JQSRT*, 112, 1323
- Wang, L., Howell, D. A., Höflich, P., & Wheeler, J. C. 2001, *ApJ*, 550, 1030
- Whalen, D. J., Even, W., Lovekin, C. C., Fryer, C. L., Stiavelli, M., Roming, P. W. A., Cooke, J., Pritchard, T. A., Holz, D. E., & Knight, C. 2013, *ApJ*, 768, 195
- Williams, G. G., Dessart, L., Hoffman, J. L., Huk, L. N., Leonard, D. C., Milne, P., Smith, N., & Smith, P. S. 2014, in *American Astronomical Society Meeting Abstracts*, Vol. 223, 354.22
- Woosley, S. E., Blinnikov, S., & Heger, A. 2007, *Nature*, 450, 390
- Zel'dovich, Y. B. & Raizer, Y. P. 1967, *Physics of shock waves and high-temperature hydrodynamic phenomena*
- Zhang, T., Wang, X., Wu, C., Chen, J., Chen, J., Liu, Q., Huang, F., Liang, J., Zhao, X., Lin, L., Wang, M., Dennefeld, M., Zhang, J., Zhai, M., Wu, H., Fan, Z., Zou, H., Zhou, X., & Ma, J. 2012, *AJ*, 144, 131